Tectonophysics 667 (2016) 87–107

Contents lists available at ScienceDirect

Tectonophysics

journal homepage: www.elsevier.com/locate/tecto

Extrusion vs. duplexing models of Himalayan mountain building 2: The South Tibet detachment at the Dadeldhura klippe

Dian He [a,*], A. Alexander G. Webb [b], Kyle P. Larson [c], Axel K. Schmitt [d]

[a] Department of Geology and Geophysics, Louisiana State University, Baton Rouge, LA 70803, USA
[b] School of Earth and Environment, University of Leeds, Leeds LS2 9JT, UK
[c] Earth and Environmental Sciences, University of BC Okanagan, Kelowna V1V 1V7, Canada
[d] Department of Earth and Space Sciences, University of California, Los Angeles, CA 90095, USA

ARTICLE INFO

Article history:
Received 25 February 2015
Received in revised form 15 July 2015
Accepted 11 November 2015
Available online 25 November 2015

Keywords:
Himalayan orogen
Tectonic model
South Tibet detachment
Duplexing
Extrusion

ABSTRACT

Himalayan mountain building has been dominantly explained by two types of models: extrusion and duplexing. To elucidate possible roles of these mechanisms during emplacement of the Himalayan crystalline core, we investigate an area speculated to contain the southern leading edge of the crystalline core: the northeastern margin of the Dadeldhura klippe, western Nepal. We found an ~700 m thick, primarily top-to-the-north shear zone within the klippe; we term this as the Tila shear zone. The shear zone occurs within a right-way-up metamorphic field gradient, and separates footwall gneiss from hanging wall schist. Similarly, deformation temperatures estimated from quartz and feldspar microstructures and quartz *c*-axis fabrics indicate a right-way-up thermal gradient of ~77–189 °C/km. U–Pb zircon dating of post-kinematic leucogranite dikes suggests that ductile shearing along the Tila shear zone occurred prior to ~17–14 Ma. We correlate the Tila shear zone to the South Tibet detachment (STD) on the basis of consistent structural fabrics (shear sense), lithologies, metamorphism, and deformation timing. This interpretation, in combination with regional constraints, indicates southwards-increasing proximity of the STD (Tila shear zone) and the Main Central thrust (MCT). These two shear zones are separated by ~3 km of structural section in the northern portion of our study area, and become close to within ~1 km of separation, in the southern portion. Interpolation suggests that the STD (Tila shear zone) and MCT merge 15 $\pm$ 10 km southwest of our study area. The increasing-to-south proximity and potential merger of the two shear zones suggest that the STD formed as a backthrust from the MCT. This interpretation contrasts with the long-standing normal fault interpretation of the STD. Because the STD and MCT bound the Himalayan crystalline core, these findings document crystalline core emplacement at depth via tectonic wedging. This kinematic evolution is consistent with duplexing, but not extrusion to the surface.

1. Introduction

Two general types of mountain-building models have been proposed to explain many phases of development of the Himalaya in response to India–Asia collision: extrusion (e.g., Burchfiel and Royden, 1985) and duplexing (e.g., Bollinger et al., 2004). The proposed extrusion models involve exhumation of mid-crustal material to the surface between surface-breaching faults, with a thrust fault below and a normal fault above (e.g., Beaumont et al., 2001; Burchfiel and Royden, 1985; Godin et al., 2006; Hodges et al., 2001). Duplexing models involve accretion of material from the underthrusting Indian plate to the over-riding orogen (e.g., Bollinger et al., 2004; Herman et al., 2010; Konstantinovskaia and Malavieille, 2005; Robinson et al., 2003; Schelling and Arita, 1991). The two model types are not mutually exclusive — material can be accreted from the down-going plate and also funneled to the surface between two bounding faults in the over-riding plate. The extrusion models do feature one exclusive aspect, however: nearly all Himalayan extrusion models require $\gg$10 km normal-sense slip along a specific structure, the South Tibet detachment (STD), which separates the Himalayan crystalline core from the lower grade overlying rocks along the length of the orogen (Fig. 1A) (e.g., Beaumont et al., 2001; Burchfiel and Royden, 1985; Burchfiel et al., 1992; Godin et al., 2001; Grujic et al., 1996; Hodges et al., 1992, 2001; Kohn, 2008; Long and McQuarrie, 2010).

In most recognized exposures, the STD occurs as a dominantly top-to-the-north, north-dipping shear zone that was active in the early and middle Miocene, and arguably even until the Pliocene to Recent (e.g., Burchfiel et al., 1992; Burg et al., 1984; Cottle et al., 2007; Hodges et al., 1992, 1996; Hurtado et al., 2001; McDermott et al., 2013; Rana et al., 2013; Searle, 2010). This geometric and kinematic pattern leads most workers to interpret the STD as a high-slip, orogen-parallel, syn-convergence normal fault, which is argued to

* Corresponding author at: Shell International Exploration and Production Inc., 3333 Hwy 6 South, Houston, TX 77082, USA.
E-mail address: dian.he@shell.com (D. He).

http://dx.doi.org/10.1016/j.tecto.2015.11.014
0040-1951/

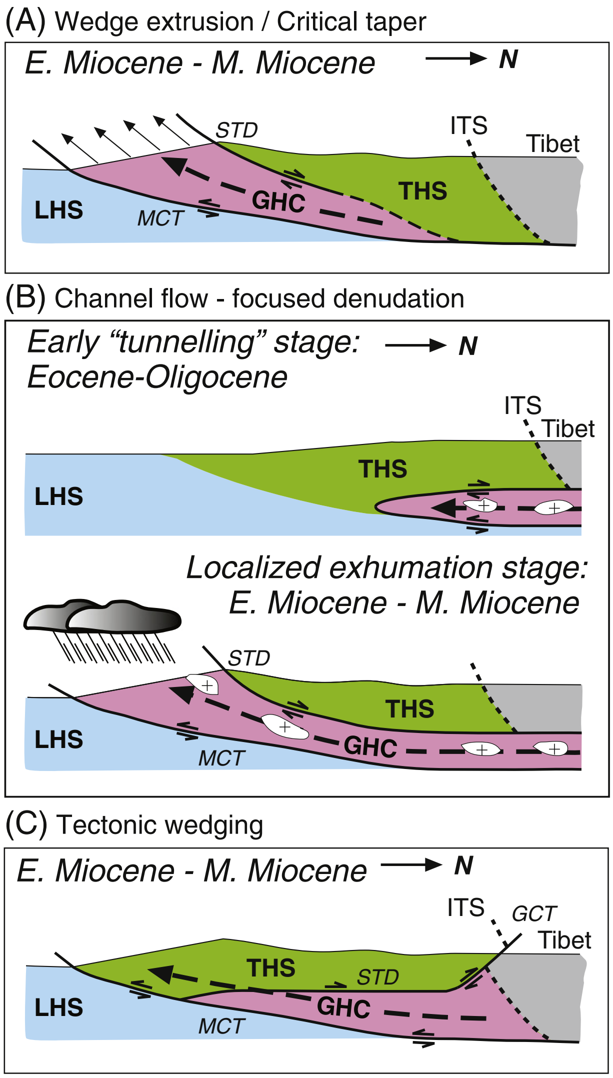

Fig. 1. Himalayan tectonic models for the emplacement of the Greater Himalayan Crystalline complex modified from Webb et al. (2011a). Note that, in the channel tunneling stage of the channel flow — focused denudation model, the STD geometry (top boundary of the tunnel) is largely flat and emanates from the basal thrust (base of the tunnel) and feeds a top-to-the-north thrust. LHS — Lesser Himalayan Sequence; GHC — Greater Himalayan Crystalline complex; THS — Tethyan Himalayan Sequence; MCT — Main Central thrust; STD — South Tibet detachment; GCT — Great Counter thrust; ITS — Indus-Tsangpo suture.

have 10s or 100s of km of slip (e.g., Cooper et al., 2012). This normal faulting concept has been widely exported to ancient orogenic belts that feature antithetic shear zones (e.g., Sevier orogen — Hodges and Walker, 1992; Wells, 1997; Grenville orogen — Selleck et al., 2005; Jamieson et al., 2007; Rivers, 2008; Canadian Cordillera — Brown and Gibson, 2006; Kuiper et al., 2006; Australia's Petermann orogen — Raimondo et al., 2009; Tanzania — Fritz et al., 2009). Such structures have not been observed in other active advancing convergence zones — perhaps the closest comparable structure is the Cordillera Blanca detachment fault of the Peruvian Andes, but this has much less slip and lateral extent (Giovanni et al., 2010).

Modeling and field-based investigation of the Himalaya over the past ~14 years have increasingly suggested that the STD may be a backthrust for part (e.g., Beaumont et al., 2001) or all (e.g., Webb et al., 2007) of its motion history. This interpretation is implicitly inherent in channel flow modeling, which shows translation of the crystalline core as a two-phase process involving (1) southwards tunneling of high-grade rocks below the STD, followed by (2) extrusion of these rocks to the surface with the STD as the upper bound of the extrusive zone (Fig. 1B) (Beaumont et al., 2001; Kellett and Grujic, 2012). During the first phase of this process, the STD is a sub-horizontal, top-to-the-north fault that emanates from the basal thrust at the leading edge of the tunnel; therefore, the geometry and kinematics of the STD are consistent with backthrusting (Fig. 1B). Similarly, synthesis of existing geometric constraints along the length of the orogen led Yin (2006) to suggest that the STD may have functioned as a backthrust for most of its history. Regional tectonic investigations in the western and central Himalaya support this view, documenting STD geometry across the southern portions of the Himalaya consistent with the root zone of a backthrust (He et al., 2015; Leger et al., 2013; Webb et al., 2007, 2011a, 2011b). A corresponding tectonic wedging model does not require any normal slip along the STD (Fig. 1C) (Webb et al., 2007).

The STD backthrust interpretation has far-reaching implications because the STD is the source of orogen-parallel, syn-convergence normal faulting concepts that have been widely applied to many other orogens. Viability of a backthrust STD model would motivate re-evaluation of syn-convergence normal faulting concepts and associated extrusion models worldwide. The backthrust model makes a clear prediction: where the crystalline core is preserved across the southern Himalaya, the STD-backthrust root zone should be similarly preserved. Here we investigate a possible root zone exposure across the northeastern margin of the Dadeldhura klippe, western Nepal, via integrated structural mapping, microstructural, quartz *c*-axis fabric, and geochronological studies.

This contribution is the second in a three-paper series, which explores the question of relative contributions of extrusive and duplexing tectonics in the Himalaya across different regions and geologic periods. The first paper (Yu et al., 2015) examines middle Miocene to Recent Himalayan deformation in NW India. The present work offers new data on the Miocene tectonics of the Main Central thrust (MCT) and STD in western Nepal and interrogates the viability of the backthrust STD model. The third paper (He et al., 2015) investigates similar questions as the present work in central Nepal, and it also incorporates recent findings of faults subdividing the crystalline core into a synthesis model showing duplexing dominating Himalayan mountain building from Oligocene to Present.

2. Geological background

2.1. Orogenic framework

At first order, the Himalayan orogen is widely recognized as a three unit-two fault stack (e.g., Hodges, 2000; Yin, 2006). The three major units of the Himalayan orogen – the Lesser Himalayan Sequence, the Greater Himalayan Crystalline complex, and the Tethyan Himalayan Sequence – have been variably defined in terms of structural positions, metamorphic grades, and stratigraphic ages (e.g., Hodges, 2000; Searle et al., 2008; Upreti, 1999; Yin, 2006). These three units are commonly considered by largely fault-based definition because of indistinguishable detrital zircon age distribution and protolith lithologies (e.g., McKenzie et al., 2011; McQuarrie et al., 2013; Myrow et al., 2003, 2009; Webb et al., 2011a, 2013; Yin et al., 2010). In this definition, the Greater Himalayan Crystalline complex is bounded by the Main Central thrust (MCT) below and the STD above; the Lesser Himalayan Sequence is the pre-Cenozoic MCT footwall, and the Tethyan Himalayan Sequence occupies the STD hanging wall (Fig. 2) (e.g., Searle et al., 2008; Yin, 2006). Within this framework, the Greater Himalayan Crystalline complex is commonly taken to be synonymous with the "crystalline core" of the orogen. Below we describe this basic framework as well as frontal klippen (such as the Dadeldhura klippe), which may be incorporated into the basic framework in one of at least five ways (Section 2.2).

There are some disagreements in the literature regarding definitions of the MCT and STD (see review of Yin, 2006). The MCT has been mapped at differing structural levels by a variety of criteria, such as a lithological contact (e.g., Heim and Gansser, 1939); differences in

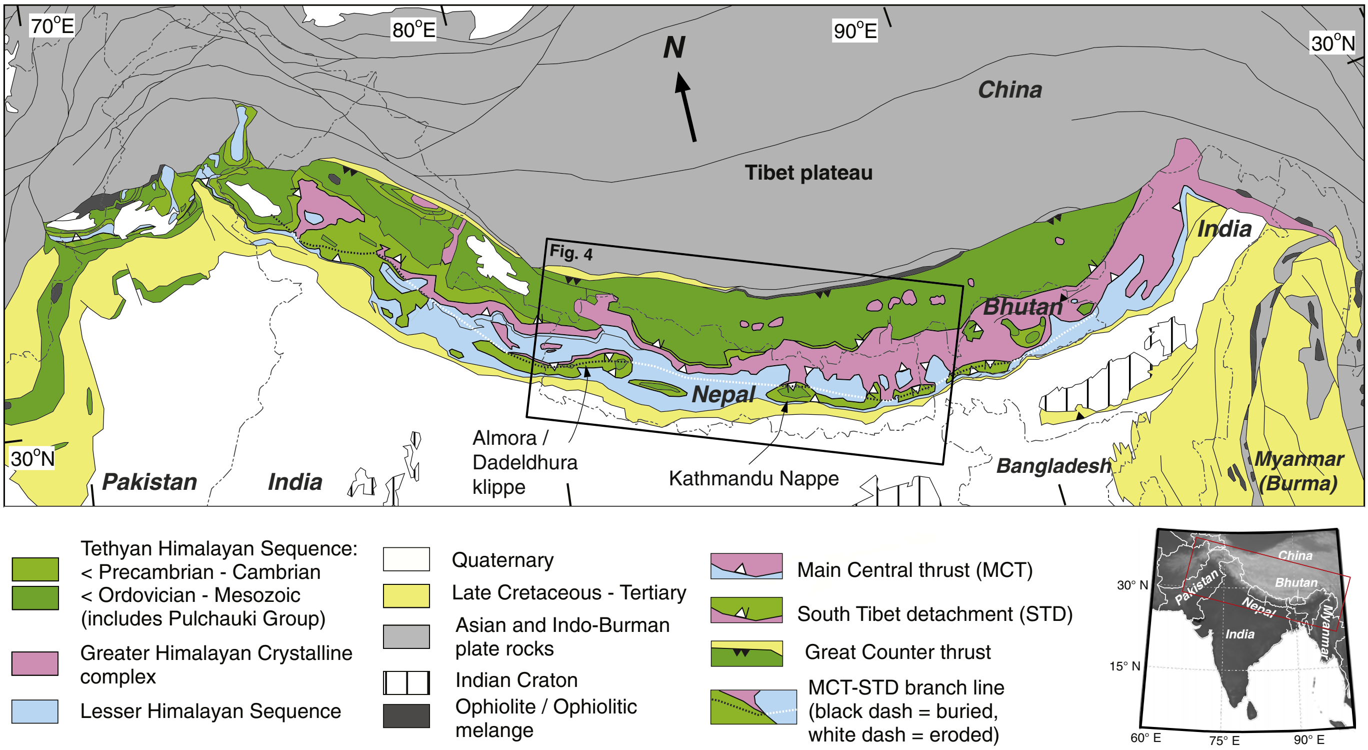

Fig. 2. Simplified tectonic map of the Himalayan orogen, based on Lombardo et al. (1993), Goscombe and Hand (2000), Murphy et al. (2009), Webb et al. (2011b) and references therein.

detrital zircon ages, isotopic ratios, and chemical element concentration across the shear zones (e.g., Girault et al., 2012; Parrish and Hodges, 1996); a distributed ductile strain zone (e.g., Searle et al., 2008); metamorphic isograd correlation (e.g., Arita, 1983); geochronological constraints (e.g., Hubbard and Harrison, 1989); and combinations of some of them (e.g., Harrison et al., 1997; Hodges et al., 1996; Le Fort, 1975; Martin et al., 2005). Similarly, the STD has been variably defined as consisting of (1) upper brittle fault(s) and a lower ductile shear zone or (2) only a ductile shear zone (e.g., Burchfiel et al., 1992; Carosi et al., 1998; Cottle et al., 2007, 2011; Godin et al., 2001; Hodges et al., 1992, 1996). Various interpreted strands of the STD at different exposures are suggested to be active during various periods spanning from early-middle Miocene (e.g., Searle et al., 2003; Kellett et al., 2009; Leloup et al., 2010; Kellett and Grujic, 2012; also see review of Godin et al., 2006) to Recent time (e.g., Hurtado et al., 2001; McDermott et al., 2013; Rana et al., 2013). In this study, we follow Webb et al. (2011a, 2011b) by identifying the MCT and STD via the spatial coincidence of three criteria: high strain (mylonitic shear zones), inverted (MCT) or right-way-up (STD) metamorphic field gradients, and activity during the early to middle Miocene. The generic shear and thermal pattern across the classic three unit-two fault stack is summarized in Fig. 3 and detailed below.

The MCT is a hundreds of meters to several kilometers thick, top-to-the-south shear zone (e.g., Le Fort, 1975). It is a continuous, passively folded structure exposed along the entire length of the orogen, and ~100 km across-strike (Figs. 2 and 4) (e.g., DiPietro and Pogue, 2004; Stöcklin, 1980; Valdiya, 1980; Yin, 2006). Although the MCT commonly juxtaposes the Greater Himalayan Crystalline complex over the Lesser Himalayan Sequence (e.g., Arita, 1983; Heim and Gansser, 1939; Le Fort, 1975), in portions of the western Himalaya the Tethyan Himalayan Sequence directly overlies the Lesser Himalayan Sequence along the MCT (Fig. 2) (e.g., Thakur, 1998; Webb et al., 2007, 2011a; Yin, 2006).

The STD is a dominantly top-to-the-north shear zone that is hundreds of meters to ~2 kilometers thick (Figs. 2 and 4) (e.g., Burchfiel et al., 1992; Burg et al., 1984; Godin et al., 2001; Herren, 1987; Hodges et al., 1996; Lombardo et al., 1993). Similar to the MCT, it extends along the length of the orogen and is possibly discontinuously exposed for as much as ~200 km across-strike (e.g., Kellett and Grujic, 2012; Larson et al., 2010a; Wagner et al., 2010; Webb et al., 2011b). Ductile

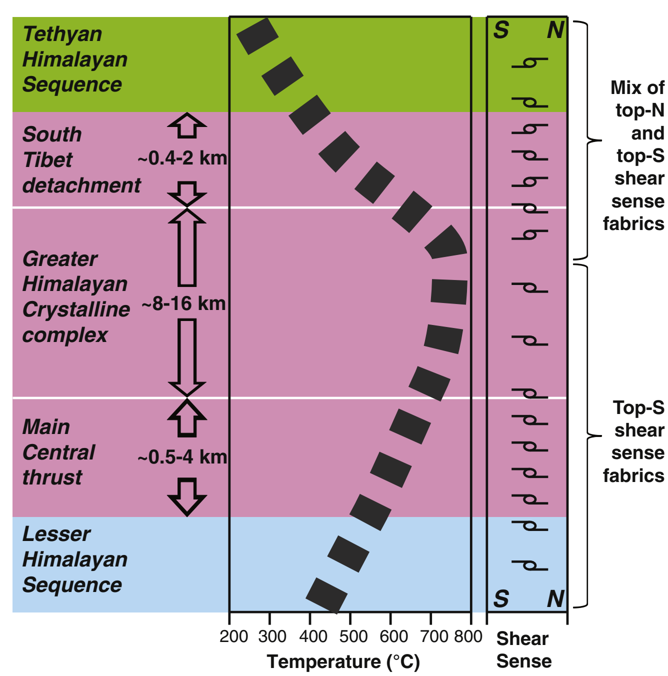

Fig. 3. Generic section across the three units and two faults showing the thermal profile and shear sense. The section shows an inverted thermal gradient across the Main Central thrust and a right-way-up thermal gradient across the South Tibet detachment in middle column, and uniform top-to-the-south shear sense from the Lesser Himalayan Sequence to upper portion of the Greater Himalayan Crystalline complex and a mix of top-to-the-north and top-to-the-south shear senses across the South Tibet detachment in right column.

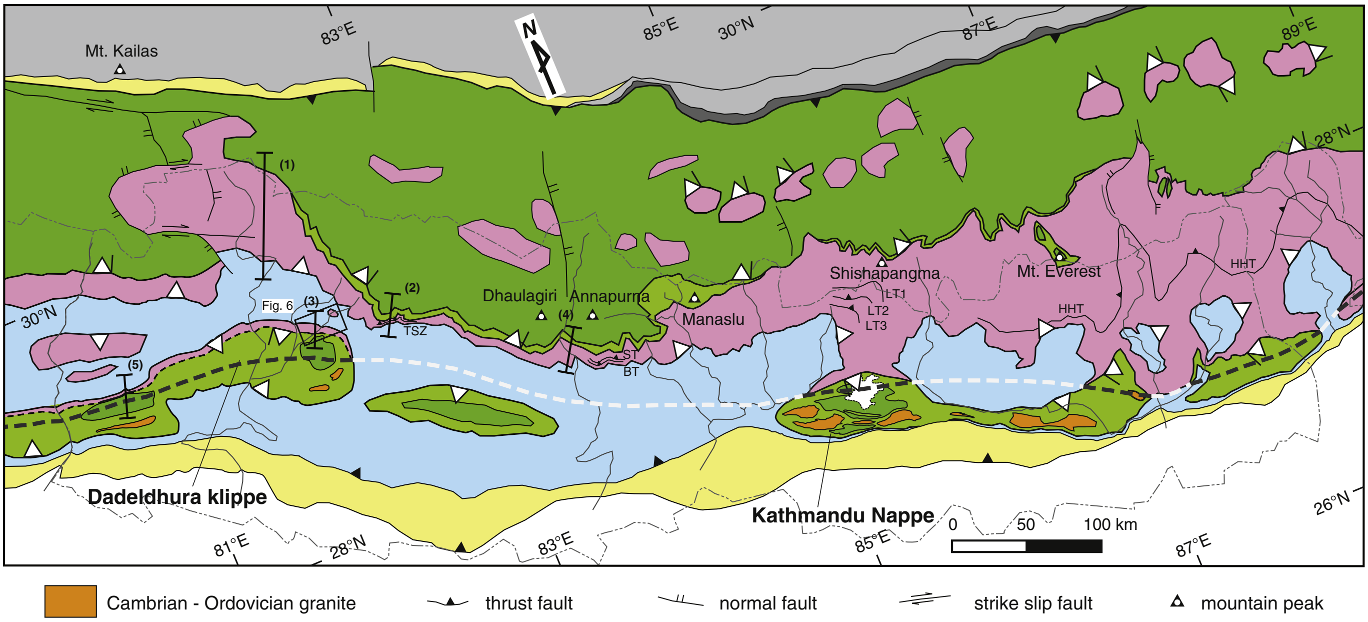

Fig. 4. Simplified geological map of the central Himalaya, units as in Fig. 2 except as specified. The area of Fig. 6 is outlined. This map is based on the integration of following work: Gurla Mandhata–Lower Dolpo region in west Nepal modified from Murphy and Copeland (2005) and Carosi et al. (2007, 2010); Dhaulagiri-Annapurna–Manaslu region modified from Hodges et al. (1996), Vannay and Hodges (1996), Searle and Godin (2003), and Martin et al. (2005); Shishapangma-Everest–Ama Drime region modified from Searle et al. (1997, 2003, 2008), Cottle et al. (2007), and Kali et al. (2010); Dadaldhura klippe region modified from Hayashi et al. (1984), Upreti (1999), DeCelles et al. (2001), Gehrels et al. (2006b), Robinson et al. (2006), and Célérier et al. (2009), and our mapping; Kathmandu region modified from Stöcklin and Bhattarai (1982), Rai et al. (1998), Johnson et al. (2001), Gehrels et al. (2006a)and Webb et al. (2011b) and our mapping; eastern Nepal and its easterly region modified from Lombardo et al. (1993), Goscombe and Hand (2000), Grujic et al. (2011), and Kellett and Grujic (2012); North Himalaya gneiss domes region modified from Lee et al. (2004), Larson et al. (2010a), King et al. (2011), Quigley et al. (2006), Wagner et al. (2010), and Zhang et al. (2012); Indus-Yalu suture zone modified from Murphy et al. (2009) and Webb et al. (2011b). TSZ — Toijem shear zone (Carosi et al., 2010); BT — Bhanuwa thrust, ST — Sinuwa thrust (Corrie and Kohn, 2011); LT1, LT2, LT3 — Langtang thrust 1, 2, 3 (Reddy et al., 1993); HHT — High Himal thrust (Goscombe et al., 2006). The bold line bars with numbers mark the transects along which the thickness of the Greater Himalayan Crystalline complex is projected in Fig. 13.

shear is ubiquitous along the structure but brittle faults are commonly absent (e.g., Cottle et al., 2007; Vannay et al., 2004; Webb et al., 2007, 2013). Therefore, brittle faulting may represent subsequent deformation unrelated to STD activity. In this study, we only consider the early to middle Miocene ductile motion to represent the STD (see review of Godin et al., 2006). The STD is a largely flat-on-flat fault contact. Sedimentary pinch-outs in Tethyan Himalayan Sequence stratigraphy (e.g., Frank et al., 1995; Thakur and Rawat, 1992; Vannay and Steck, 1995) lend it the appearance of cutting up-section in the hanging wall in some regions (see discussion in He et al., 2015), whereas a gneiss complex with Late Proterozoic through Ordovician protolith ages and Tertiary leucogranitic intrusions uniformly dominates the footwall. Proposed slip estimates along the STD vary from ~35 km up to as much as 190 km (e.g., Antolin et al., 2013; Burchfiel et al., 1992; Cooper et al., 2012, 2013; Cottle et al., 2007; Kellett and Grujic, 2012). These numbers are stated as minimum slip estimates, based on distances between the southernmost and northernmost exposures of the STD in various regions across the orogen. The approach assumes that the STD yields pairs of hanging wall and footwall cutoffs, and because no cutoffs are unambiguously observed (controversial relationships exist in Bhutan, compare Long and McQuarrie, 2010 versus Webb et al., 2011b), cutoffs are thought to have been eroded and/or buried beyond the exposed traces of the fault. However, given the dominant layer-parallel nature of the structure, it may be that no stratigraphic fault cutoffs exist, which would preclude derivation of meaningful slip estimates using this approach (Yin, 2006).

An inverted metamorphic field gradient characterizes rocks across the MCT (e.g., Harrison et al., 1999; Hodges et al., 1996; Le Fort, 1975; Vannay and Hodges, 1996; Yin, 2006). The inverted gradient persists from the upper Lesser Himalayan Sequence to the middle Greater Himalayan Crystalline complex. In contrast, the upper Greater Himalayan Crystalline complex, the STD, and the Tethyan Himalayan Sequence rocks feature a right-way-up metamorphic field gradient. Peak temperatures increase from ~550–600 °C in the Lesser Himalayan Sequence immediately below the MCT to ~700–850 °C in the Greater Himalayan Crystalline complex with a lack of metamorphic grade break across the MCT in most of regions (Fig. 3) (e.g., Daniel et al., 2003; Jamieson et al., 2004; Kohn et al., 2001; Pêcher, 1989; Searle et al., 2003; Spencer et al., 2012; Vannay et al., 1999). The base of the MCT zone is generally characterized by a peak metamorphic temperature of ~600 °C (e.g., Catlos et al., 2001; Hubbard, 1989; Kohn et al., 2001; Vannay and Grasemann, 1998; Vannay and Hodges, 1996; Vannay et al., 2004). Similarly, the cold-over-hot thermal pattern across the STD also exhibits a gradual transition. Peak metamorphic temperatures decrease smoothly from ~750–650 °C to ~450–250 °C across km-scale sections from the STD footwall, through the STD shear zone, into the STD hanging wall (e.g., Crouzet et al., 2007 (central-western Nepal); Jessup et al., 2008 (the Mt. Everest area); Kellett et al., 2010 (Bhutan); Cottle et al., 2011 (Dzakaa Chu, the Mt. Everest area); Law et al., 2011 (Rongbuk, the Mt. Everest area); Kellett and Grujic, 2012 (Bhutan); Leger et al., 2013 (NW India)). Some areas show breaks in the metamorphic transition across the top of the crystalline core: these sharp transitions may be caused by (1) STD upper brittle fault(s) or (2) younger east–west extending normal faults (see discussions in Cooper et al., 2013 and Webb et al., 2013, respectively). The basal STD zone displays ~600–650 °C peak metamorphic temperature along the main trace (e.g., Chambers et al., 2009; Coleman, 1998; Cottle et al., 2011; Hodges et al., 1992; Jessup et al., 2008; Kellett et al., 2009; Law et al., 2011; Leloup et al., 2010; Searle et al., 2003), and records roughly constant temperature on multiple STD exposures extending up to 200 km in its transport direction from the North Himalayan gneiss domes in the north to the STD klippen in the south (e.g., Jessup et al., 2008 (the Mt. Everest area — a middle strand along the crest of the orogen); Kellett et al., 2010 (STD klippe in Bhutan — a southern strand in the front of the orogen); Wagner et al., 2010 (Kangmar dome, one of the North Himalayan gneiss domes — a northern strand in the hinterland)).

The Lesser Himalayan Sequence contains Paleoproterozoic to Cambrian low-grade metasedimentary rocks and overlying Permian to Cretaceous Gondwana strata (e.g., DeCelles et al., 2001; Gansser, 1964; Le Fort, 1975). Greater Himalayan Crystalline complex protoliths are dominantly Neoproterozoic metasedimentary rocks intruded by Cambrian-Ordovician granite (DeCelles et al., 2000; Hodges et al., 1996; Parrish and Hodges, 1996). These rocks occur as high-grade kyanite- and sillimanite-bearing gneiss, schist, and migmatite, intruded by Tertiary leucogranite (e.g., Hodges et al., 1996; Le Fort, 1975, 1996; Searle et al., 1997). In the central Himalaya, the Greater Himalayan Crystalline complex can be divided into two sections: paragneiss in the lower level and calc-silicate with thin interlayers of granitic gneiss in the upper level (e.g., Carosi et al., 2010; Corrie and Kohn, 2011; Hodges et al., 1996; Le Fort, 1975; Searle and Godin, 2003; Vannay and Hodges, 1996). The Tethyan Himalayan Sequence mainly comprises basal Neoproterozoic-Cambrian psammitic and pelitic schist and phyllite and overlying Ordovician to Mesozoic strata (e.g., Garzanti, 1999; Godin, 2003; Godin et al., 2001). The Neoproterozoic–Cambrian metasedimentary rocks are locally intruded by Paleozoic granite and may share protolith layers with the Greater Himalayan Crystalline complex (e.g., Miller et al., 2001; Vannay et al., 2004; Webb et al., 2011a). These rocks are termed the Everest Series (or North Col Formation) in eastern Nepal (e.g., Godin et al., 2001; Lombardo et al., 1993; Myrow et al., 2009; Searle et al., 2003), the Haimanta Group in northwestern India (e.g., Chambers et al., 2009; Webb et al., 2011a), and the Chekha Group in Bhutan (e.g., Grujic et al., 2002). The Ordovician–Mesozoic strata comprise low-grade and unmetamorphosed carbonate and siliciclastic rocks (Crouzet et al., 2007; Godin, 2003).

2.2. Lesser Himalayan Crystalline Nappes

Erosional remnants of a thrust sheet placed southwards atop the Lesser Himalayan Sequence in the frontal portions of the orogen are termed the Lesser Himalayan Crystalline Nappes (e.g., Stöcklin, 1980; Upreti, 1999). The Dadeldhura klippe and Kathmandu Nappe are the most prominent Lesser Himalayan Crystalline Nappes in the central Himalaya (Fig. 4). These klippen largely consist of the Bhimphedi Group and Phulchauki Group (Gehrels et al., 2006a, 2006b; Stöcklin, 1980; Upreti and Le Fort, 1999). The Bhimphedi Group is composed of medium- to high-grade metasedimentary rocks with Neoproterozoic protoliths intruded by Cambrian-Ordovician granite (e.g., DeCelles et al., 1998; Johnson et al., 2001). The overlying Phulchauki Group, exposed at the center of the klippe synforms, consists of Ordovician–Devonian low-grade and unmetamorphosed sedimentary rocks. The Phulchauki Group is commonly correlated to the Tethyan Himalayan Sequence rocks of the same ages, whereas the affiliation of the Bhimphedi Group remains debated (DeCelles et al., 2001; Funakawa, 2001; Gehrels et al., 2003, 2006a, 2006b; Johnson et al., 2001; Robinson et al., 2006; Stöcklin, 1980; Upreti, 1999; Upreti and Le Fort, 1999; Webb et al., 2011b). Depositional contacts are widely perceived to separate the Bhimphedi Group and Phulchauki Group (e.g., DeCelles et al., 2001; Gehrels et al., 2006a, 2006b; Hayashi et al., 1984; Johnson et al., 2001; Robinson et al., 2006), but this is not universally agreed upon, as discussed below. High grade rocks, termed the Sheopuri Gneiss, locally occur along the basal northern margins of the Lesser Himalayan Crystalline Nappes (e.g., Rai et al., 1998).

The Lesser Himalayan Crystalline Nappes were emplaced along a thrust contact that is almost universally interpreted as the MCT (e.g., Yin, 2006). Locally, this contact has been termed the Dadeldhura thrust in the Dadeldhura klippe and Mahabharat thrust in the Kathmandu Nappe (e.g., Johnson et al., 2001; Robinson et al., 2006). The ~1–2 km thick basal shear zone displays an inverted metamorphic field gradient, whereas the bulk of the klippen are generally characterized by right-way-up metamorphic field gradients (e.g., DeCelles et al., 2001; Johnson et al., 2001).

Five different models for the structural geometry of the Lesser Himalayan Crystalline Nappes have been put forward.

(1) The STD is interpreted to cut upsection to the north of (and structurally above) the Lesser Himalayan Crystalline Nappes (Fig. 5A) (e.g., Gehrels et al., 2003; Johnson et al., 2001; Long and McQuarrie, 2010).
(2) The Bhimphedi Group–Phulchauki Group contact may be the southern continuation of the STD (Fig. 5B) (Antolin et al., 2013; Yin, 2006).
(3) The bulk of the Lesser Himalayan Crystalline Nappes may represent distinct thrust sheets structurally below the MCT (Fig. 5C) (e.g., DeCelles et al., 1998, 2001; Rai et al., 1998; Srivastava and Mitra, 1994; Upreti and Le Fort, 1999). In such models, the MCT separates the Bhimphedi Group to the south from the Sheopuri Gneiss to the north (the latter is taken as equivalent to the Greater Himalayan Crystalline complex).

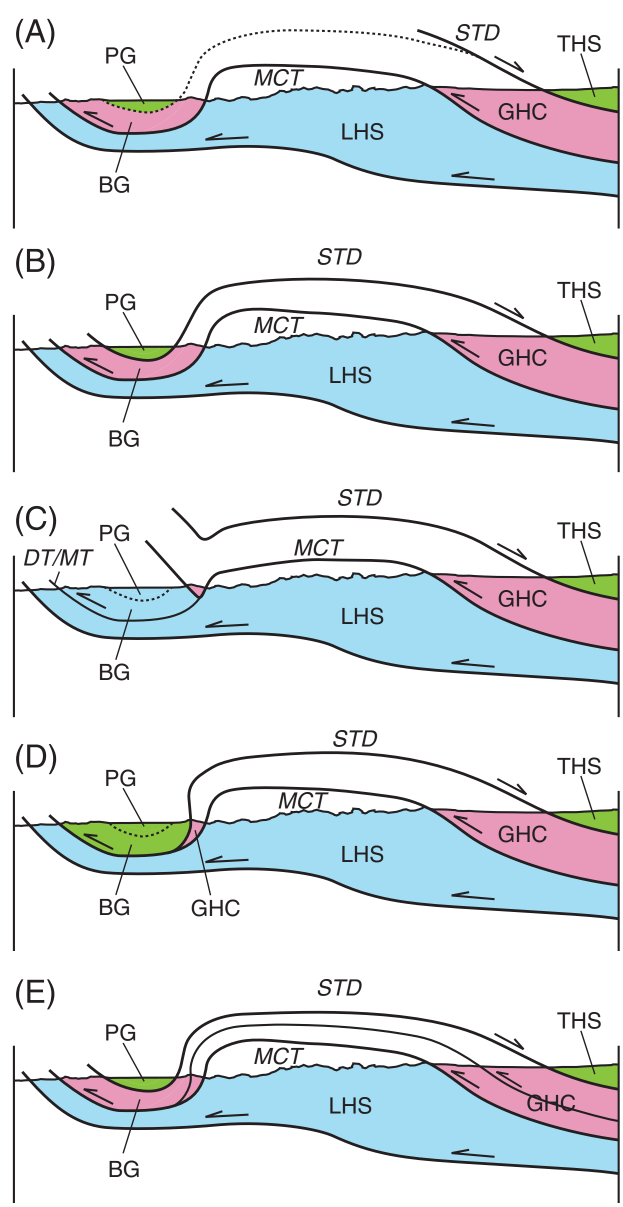

Fig. 5. Models for the frontal klippen in the central Himalaya. Bold lines are major shear zones (STD and MCT); thin solid lines are second-order faults; dashed lines depositional contacts. Abbreviation is the same as in Fig. 1 except as specified. BG — Bhimphedi Group; PG — Phulchauki Group. See text for details.

(4) The southern portion of the STD may occur along the northern margins of the Lesser Himalayan Crystalline Nappes (Fig. 5D) (He et al., 2015; Webb et al., 2011b). In this model, the STD separates the Bhimphedi Group from the Sheopuri Gneiss, and the southern termination of this contact along the basal shear zone of the Lesser Himalayan Crystalline Nappes is interpreted as the STD root zone along the MCT. This interpretation led Webb et al. (2011b) to predict that a MCT–STD branch line occurs in frontal portions of the orogen, including the focus area of the present study (Figs. 2 and 4).

(5) The Bhimphedi Group–Phulchauki Group contact may be the southern continuation of the STD and the Bhimphedi Group–Sheopuri Gneiss contact may be the southern continuation of an intra-Greater Himalayan Crystalline complex thrust (Fig. 5E) (Khanal et al., 2015).

Our investigation of shearing structures, metamorphic grades, and timing of shearing structures along the northeastern margin of the Dadeldhura klippe allows us to test the Lesser Himalayan Crystalline Nappe models via the distinct predictions for the Bhimphedi Group–Sheopuri gneiss contact. The first two models predict that this contact occurs within the Greater Himalayan Crystalline complex without structural significance, the third and fifth models predict that it is a top-to-the-south shear zone, and the fourth model predicts that it is a top-to-the-north shear zone (Fig. 5).

3. Field observations

Field mapping along the Tila River transect extends ~20 km across the northeastern limit of the Dadeldhura klippe (Fig. 6). We walked the transect and made observations at nearly every accessible outcrop. Exposure spacing varies from 100s of meters to 1–2 km, because most of the bedrock exposures are covered by vegetation and/or thick river deposits associated with the Tila River. Some of the accessible exposures (of 10s to a few 100s m in length) can be observed along roadcuts, while some with modest outcrop size (a few to 10s of meters) are spotted among the vegetation. No continuous exposures extend over ~1 km southwest of Jumla along this transect (Fig. 6). The transect passes from the MCT footwall (here, quartzite and phyllite) in the northeast; through the MCT shear zone (garnet mica schist and kyanite-bearing gneiss), a slice of high-grade metamorphic rocks (including kyanite-bearing paragneiss, calc-silicate, and migmatite), a top-to-the-north shear zone (developed across calc-silicate and garnet-biotite gneiss with granitic gneiss interlayers); and into the Bhimphedi Group (biotite schist and quartzite) in the southwest. Deformed rocks commonly display schistose foliation and gneissic banding. However, sparse lineations were observed, perhaps because (1) lineation is not widely developed in the high-grade schist and gnessic rocks in this area, and/or (2) lineation is more readily obscured than foliation, particularly gneissic foliation, by intense weathering. The second causative factor is more likely because of the particulars of the studied rocks. The observed stretching lineation is characterized by aggregates of mm-scale, elongated /aligned (nearly one-dimensional) minerals, whereas the foliation is commonly characterized by cm-scale gneissic banding. In weathered rocks, the foliation is readily detectable by color differences, but the lineation is commonly not detectable. We interpret changes in foliation and bedding orientations across the dominantly SW-dipping northeast limb of the Dadeldhura klippe to document a km-scale, southwest-vergent, slightly overturned anticline in the MCT hanging wall. We term this structure the Jumla anticline. Because recognition of this proposed structure involves a relatively high degree of interpolation, we leave further exploration of it to the Discussion section below.

The MCT footwall is largely composed of quartzite, chloritic phyllite/schist, and metabasite. Foliation defined by muscovite and quartz gently dips to the southwest and northeast (Fig. 6).

The MCT here is an ~1200 m thick shear zone. All micro-scale and meso-scale structures are consistent with top-to-the-south sense of shear. Rocks in the lower part of the MCT shear zone are garnet–mica schist with quartzite interlayers. The upper part of the MCT shear zone consists of paragneiss and mylonitic calc-silicate. Structural fabrics in this part include mica-defined foliation, S–C fabrics, and sigma-type porphyroclasts in garnet mica schist, tight folds in quartzite interlayers, and folds and gneissic banding in paragneiss. Foliation of these rocks generally dips to the southwest. Rotated garnet and mica fish (seen via thin sections) as well as sigma-type porphyroclasts (seen in thin section and at outcrop) occur in garnet mica schist, while kyanite-bearing paragneiss and deformed leucosome segregates present asymmetric folds (Fig. 7A, B; also Fig. S1A, B). Metamorphic grade increases up-section from the garnet-in isograd through the kyanite-in isograd across the MCT zone (Fig. 6). Note that another small MCT klippe is exposed ~5 km NE of Jumla village (Fig. 6), and that only the basal MCT shear zone rocks are preserved in this klippe. Carosi et al. (2007, 2010) mapped a similar structure in this area.

In the immediate MCT hanging wall, an ~1300 m thick section consists of kyanite-bearing paragneiss and calc-silicate intruded by tourmaline-bearing leucogranite (also see Hayashi et al., 1984). Structural fabrics of these rocks are dominated by foliation and gneissic banding, which dip steeply (67–70°) to the southwest or northeast (Fig. 6) at the top of this section close to the Tila shear zone (see below).

Farther south, an ~700 m thick section consists of strongly deformed calc-silicate, garnet biotite gneiss and augen gneiss interlayers; we term this newly discovered shear zone as the Tila shear zone. Most structures in the Tila shear zone indicate a top-to-the-north sense of shear (Fig. 7D; also Fig. S1D, E) with a few exceptions showing top-to-the-south shearing (Fig. 7C; also Fig. S1C). We were not able to determine the sequence of development of the two sets of shearing structures because of the poor exposure. Sigma-type porphyroclasts and rotated porphyroclasts are widely developed across the shear zone (Fig. 7C, D; also Fig. S1C–E). The porphyroclasts in the section yield both top-to-the-north and top-to-the-south shearing. Rocks generally exhibit distinctively north-dipping foliation (Fig. 6).

Rocks south of the Tila shear zone contain calc-silicate, biotite schist, quartzite, and quartz arenite with leucogranitic intrusion. A kyanite-in isograd appears in this section again, indicating metamorphic grade drops southwards across the Tila shear zone. This kyanite-in isograd is immediately south of and roughly parallel to the Tila shear zone (Fig. 6). Deformed quartzite exhibits meter-scale upright folds. Rocks immediately south of the Tila shear zone are characterized by foliation defined by biotite and quartz, whereas primary bedding is preserved in higher level rocks. In the center of the klippe, there are large exposures of undeformed to weakly deformed granite, which are Cambrian–Ordovician in age (DeCelles et al., 1998). These lithologic, metamorphic, and structural patterns are consistent with the Bhimphedi Group which dominates the Lesser Himalayan Crystalline Nappes (e.g., Gehrels et al., 2006a, 2006b; Stöcklin, 1980; Upreti and Le Fort, 1999).

4. Deformation temperatures constrained by microstructures

4.1. Methods

Dynamic recrystallization characteristics of mineral grains can reflect the conditions, such as temperature, strain rate, and water weakening, that rocks experienced during deformation (e.g., Hirth and Tullis, 1992; Stipp et al., 2002a, 2002b). If the effects of strain rate and water weakening are assumed to be minor, or at least invariant in the studied rocks, temperature becomes the primary control on observed microtextural changes (Law, 2014). We apply the Stipp et al. (2002a, 2002b) approach of estimating relative deformation temperatures from microstructures of quartz recrystallization to assess the thermal profile in our transect.

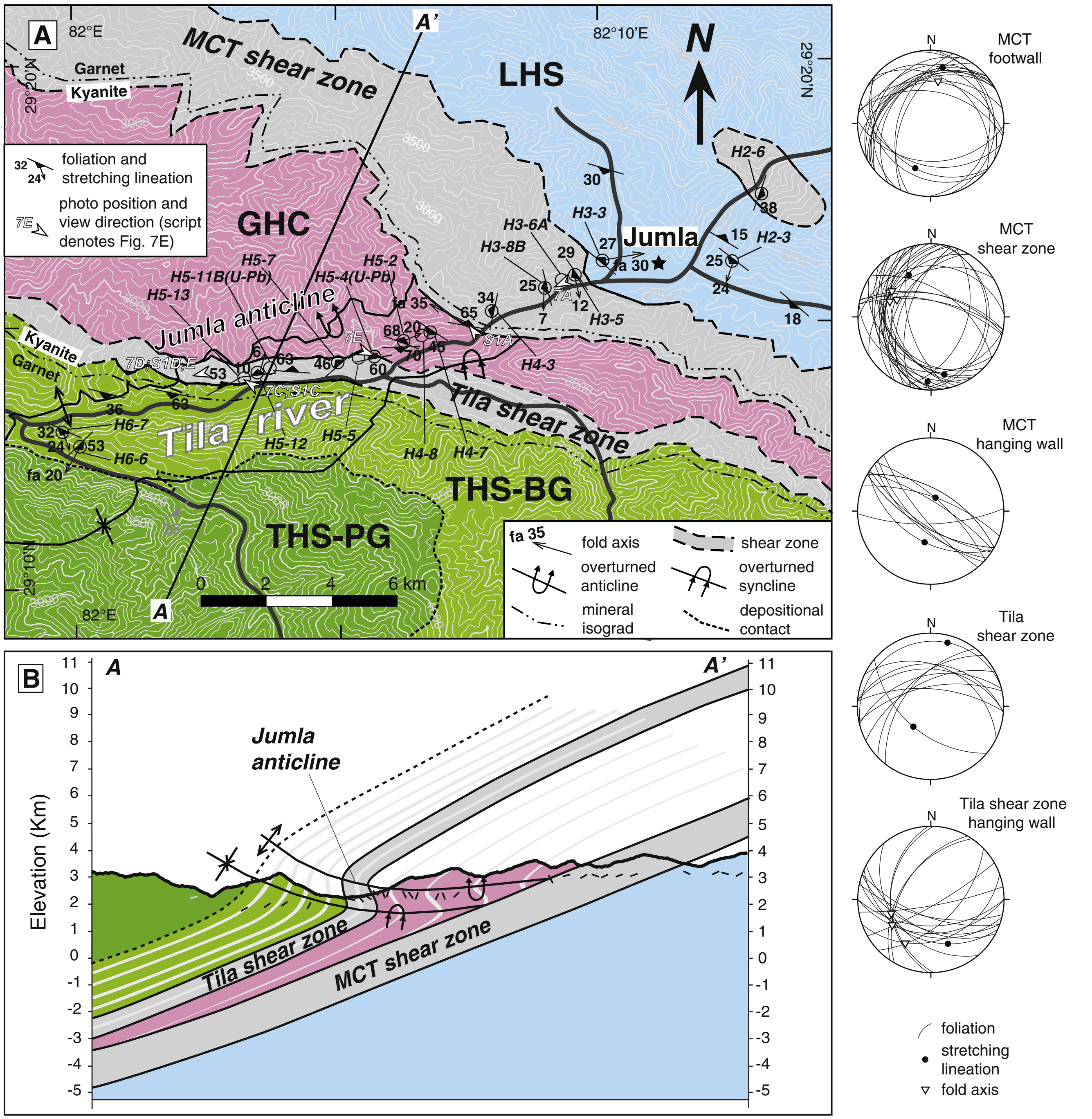

Fig. 6. (A) Geological map of the Northeastern Dadeldhura klippe with lower hemisphere equal area projection of structural data, modified from Hayashi et al. (1984) and our mapping. Abbreviation is the same as in Figs. 1 and 5. (B) Sketch cross section of line A–A′. The location of the cross section is shown in (A). The gray structural datum in the Phulchauki Group is from Hayashi et al. (1984). Note that dominant foliation, as shown in the section, is associated with (and parallel to) the shear planes of major structures.

Deformation microstructures in quartz are generally classified into three regimes (Hirth and Tullis, 1992): bulging (BLG), subgrain rotation (SGR), and grain boundary migration (GBM) recrystallization. The approximate correlation between these recrystallization regimes and temperatures has been investigated by Stipp et al. (2002a, 2002b) who suggest that BLG dominates between 300 and 400 °C, SGR dominates between 400 and 500 °C, and GBM recrystallization (GBM I at 500–~600 °C and GBM II at ~600–700 °C) dominates at higher temperatures. Many previous workers have used the Stipp et al. (2002a) microstructure thermometer to compare microstructures to metamorphic temperatures derived by mineral thermometers across the Himalayan orogen (e.g., Antolin et al., 2013; Célérier et al., 2009; Larson and Godin, 2009; Larson et al., 2010a, 2010b; Law et al., 2004, 2011, 2013; Leger et al., 2013; Long and McQuarrie, 2010; Long et al., 2011; Yakymchuk and Godin, 2012). We recognize, however, that the background geologic characteristics in our study are different from Stipp et al.'s and that multiple factors can exert influence on the development of microstructures (e.g., Law, 2014; Stipp et al., 2002a, 2002b).

Law (2014) summarizes that remarkable along-strike consistency of microstructures across the MCT exists for ~1500 km along the orogen, and suggests, based on the correlation of quartz recrystallization regimes and available metamorphic temperatures, that BLG, SGR, and GBM recrystallization across the MCT shear zone occurred at temperatures of ~350–450, 450–550, and 550–>650 °C, respectively. Given the

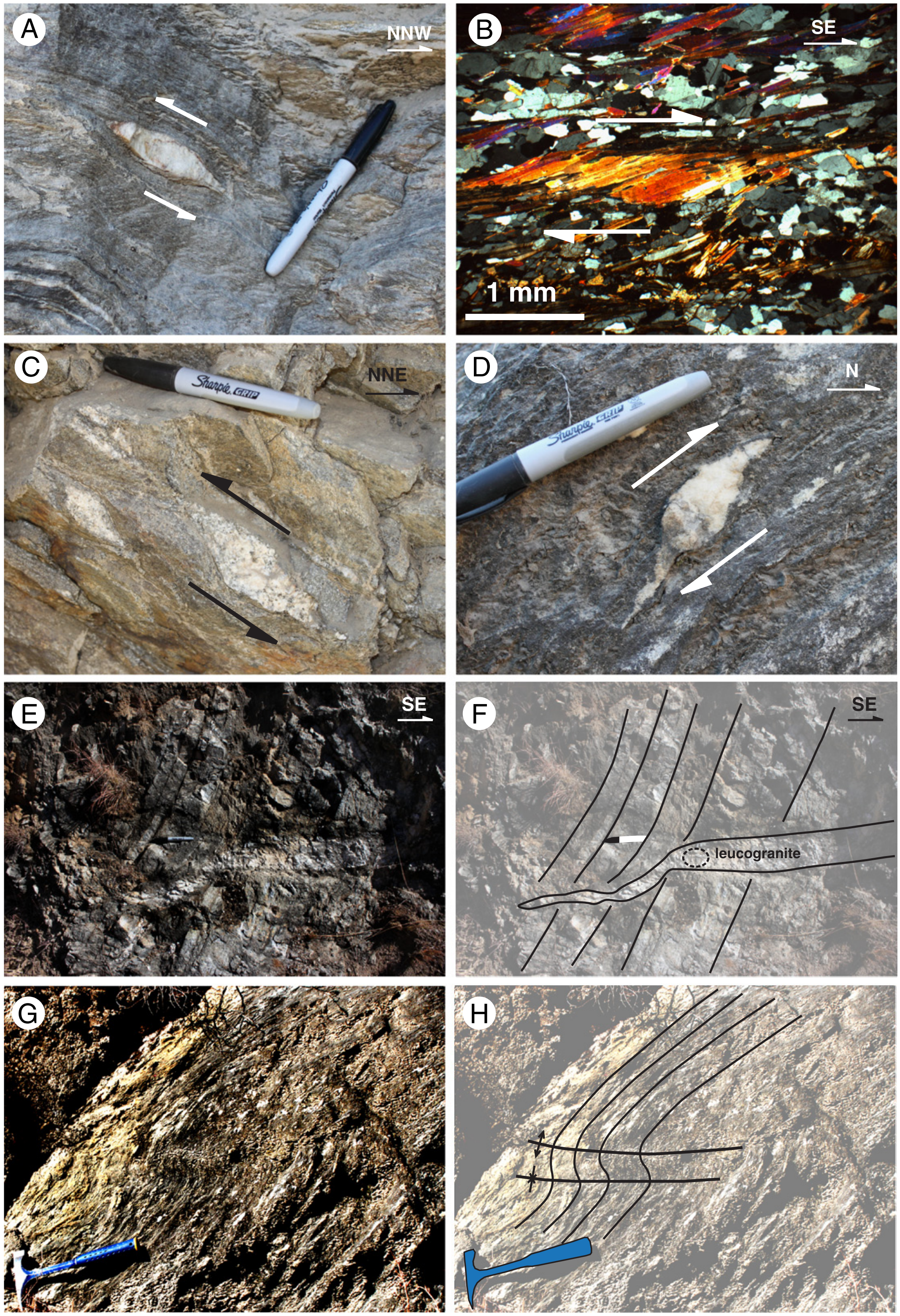

Fig. 7. Photo(micro)graphs of deformation fabrics along the Tila River transect in the northeastern Dadeldhura klippe. Locations are marked in Fig. 6. (A) Photograph of a sigma-type porphyroclast in mica schist showing top-to-the-south shearing. (B) Sample H2-6: photomicrograph of mica fish in garnet two mica schist showing top-to-the-southeast shearing. Thin sections cut perpendicular to foliation and parallel to lineation. This sample, located ~5 km north of Jumla, is interpreted as a small klippe of the MCT zone, which was also mapped by Carosi et al. (2007). Locations of photographs (A) and (B) are in the MCT shear zone. (C) Photograph of a sigma-type porphyroclast showing top-to-the-south shearing. (D) Photograph of a sigma-type porphyroclast showing top-to-the-north shearing. (E–F) Contrast-enhanced photograph and line diagram of a cross-cutting leucogranite dike. Dashed ellipse indicates leucogranite sample H5-4 to be dated. Locations of photographs (C)–(F) are in the Tila shear zone. (G–H) Contrast enhanced photograph and line diagram of a fold in the Tila shear zone.

consistent microstructures across the MCT and consistent correlation between quartz recrystallization regimes and metamorphic temperatures in multiple locations along the orogen, we follow *Law's* correlation of temperatures and quartz microstructures to guide our interpretation below. In addition, we further distinguish higher temperature GBM microtextures that include evidence of chessboard extinction. Following previous work, we interpret such fabrics to indicate deformation temperatures in excess of at least 600 °C (Lister and Dornsiepen, 1982) and likely 650 °C (see Kruhl (1998) thermometer and modification by Morgan and Law (2004)). Moreover, the deformation temperatures estimated from microstructures in this section are compared with those inferred from quartz *c*-axis fabric opening angles (see the next section and Discussion section), which, while still subject to a number of assumptions, have been shown to be relatively consistent with independent temperature estimates across the Himalaya (as summarized in Law, 2014). This comparison of temperature estimates helps reduce some of the uncertainty of using a single estimation alone. Nonetheless, we emphasize that we only treat the relative temperature trend with confidence, and all individual absolute temperatures in this and next sections must be viewed with caution.

Deformation microstructures in feldspar can also be used to help constrain deformation temperatures. For instance, K-feldspar core–mantle structures and myrmekite growth on the margins of feldspar porphyroclasts are indicative of deformation temperatures over 600 °C (Passchier and Trouw, 2005). Such textures are also used to help inform deformation temperature interpretations.

4.2. Results

Samples H2-3[1] and H3-3 are quartzite from the MCT footwall (i.e., the Lesser Himalayan Sequence) (Fig. 6). They contain recrystallized fine-grained equigranular quartz with a shape-preferred orientation that defines a foliation (Fig. S2A). Quartz in these two samples is recrystallized predominantly by subgrain rotation recrystallization (Fig. 8A), indicating temperatures of 450–550 °C.

Samples H3-5C, H3-6A, H3-8B, and H4-3 are quartzite from the MCT shear zone (Fig. 6). Quartzite of H3-5C is composed of fine-grain recrystallized quartz with irregular, yet planar grain boundaries. Quartz in this sample displays pinning structures (Fig. 8B). Two stages of the geometric relationship of mica inclusions and quartz can be seen: an initial stage of a mica inclusion completely enclosed in a quartz grain and later stage of pinning structures caused by quartz grain boundary migration (Jessell, 1987). Pinning structures are consistent with GBM recrystallization at 550–650 °C, while the straight grain boundaries indicate some static recrystallization and grain boundary area reduction. Quartz in H3-6A shows a bimodal grain size distribution (Fig. S2B). In both the small-grain and large-grain domains, quartz has a similar inequigranular texture with lobate grain shapes. The bimodal grain size distribution may reflect varying distance between mica-rich layers impeding further grain-size growth (Stipp et al., 2002a). Chessboard extinction (e.g., Mainprice et al., 1986) is observed locally (Fig. S2C). These textures together document deformation temperatures of 550–>650 °C. Quartz in H3-8B shows an inequigranular texture, often with lobate grain shapes (Fig. 8C). The texture and its lobate nature are indicative of the GBM regime with deformation temperatures at 550–650 °C. Sample H4-3 displays an inequigranular texture with irregular grain boundaries (Fig. S2D). The slightly elongate quartz grains and mica define the foliation. The texture of this sample indicates GBM recrystallization at 550–650 °C.

Samples H4-7, H4-8B, and H4-8C are from the section between the MCT and Tila shear zone (Fig. 6). Sample H4-7 is paragneiss and contains quartz that exhibits chessboard extinction (Fig. 8D), indicating that the rock experienced recrystallization at deformation temperatures of >650 °C. Sample H4-8B is leucogranite, which exhibits a K-feldspar core–mantle structure with myrmekite growing on the margin of the K-feldspar porphyroclast (Fig. S2E). The feldspar microstructures indicate that the deformation temperature have reached >600 °C (e.g., Kruse et al., 2001; Passchier and Trouw, 2005; Pryer, 1993). Moreover, growth of myrmekite on the porphyroclast margin parallel to the foliation documents deformation processes under high temperatures (e.g., Simpson and Wintsch, 1989). Sample H4-8C is also leucogranite. Quartz in this sample displays an inequigranular texture with amoeboid grain boundaries (Fig. S2F), indicating the GBM regime and deformation temperatures of 550–650 °C.

Samples H5-4, H5-5, H5-7, H5-12, and H5-13 are from the Tila shear zone (Fig. 6). Sample H5-4 is leucogranite. Flame-perthite and fractures are abundant in K-feldspar (Fig. S2G), indicating that it was subject to deformation temperatures up to ~600 °C (Passchier and Trouw, 2005; Pryer, 1993). Sample H5-5 is mylonitized garnet-bearing leucogranite. Micas and quartz are aligned to form mineral stretching lineations that plunge at 56° to the SSW direction. Quartz in this sample comprises large recrystallized grains with amoeboid grain boundaries (Fig. 8E), consistent with regime GBM and deformation temperatures of 550–650 °C. Sample H5-7 is an orthogneiss. It displays chessboard extinction in multiple quartz grains and monomineralic quartz ribbons (Fig. S2H). The chessboard extinction indicates recrystallization at >650 °C, and the monomineralic quartz ribbons are subject to be also formed in mylonitic shear zone at high-grade metamorphic conditions (e.g., Hanmer et al., 1995; Passchier and Trouw, 2005; Whitmeyer and Simpson, 2003). Sample H5-12 and H5-13 are kyanite-bearing garnet biotite gneiss. The quartz in these two samples exhibits an inequigranular texture with amoeboid grain boundaries (Fig. S2I). This texture is consistent with regime GBM and deformation temperatures of 550–650 °C.

Samples H6-6 and H6-7 are from the Tila shear zone hanging wall (Fig. 6). Sample H6-6 is biotite schist that shows an equigranular texture with small grain sizes (Fig. S2J), indicating that it is subject to regime SGR with deformation temperatures of 450–550 °C. Sample H6-7 is meta-arenite also from the Tila shear zone hanging wall. It contains small recrystallized quartz grains around large relict grains (Fig. 8F). This texture indicates that it is formed by BLG recrystallization at deformation temperatures of 350–450 °C.

5. Quartz *c*-axis fabrics

5.1. Methods

In deformed quartz-rich rocks, quartz can develop a *c*-axis preferred orientation fabric. The resultant fabric patterns may be used to assess the deformation history of the rocks in multigrain quartz-rich aggregates (e.g., Law, 1990; Lister and Hobbs, 1980; Lister and Price, 1978; Schmid and Casey, 1986). Quartz *c*-axis fabric analysis was conducted using a Russell-Head Instruments G50 automated fabric analyzer housed at the University of Saskatchewan. Fabrics produced from similar or identical instruments have proven indistinguishable from those determined through electron back-scattered diffraction (e.g., Peternell et al., 2010; Wilson et al., 2007). All thin sections analyzed were cut perpendicular to foliation and parallel to mineral stretching lineation where observed or a NE–SW direction, the approximate interpreted transport/elongation direction, if no lineation was observed. Quartz *c*-axis orientation data are plotted in equal area lower-hemisphere stereographic projection. Contour and scatter plots were generated using STEREONET 7.2.4 developed by R.W. Allmendinger (2012).

Because acquired fabric information is three dimensional, the method provides a check on the validity of the assumed elongation direction for specimens where no reliable lineation was observed. If a thin section is not cut (sub-)parallel to the elongation direction, any *c*-axis fabric yielded will not cross at the center of the stereonet. All fabrics extracted as part of this study center on the middle of the stereonet (Fig. 9), confirming that the analyzed rocks were cut (sub-)parallel to the elongation/transport direction.

All samples are described below in order of increasing structural elevation.

[1] In this paper, we present our samples with short-form names that are easy-to-read and informative. The correlation of the short-form and original names is (H)(Day)-(#) for (DH)(Month)-(Day)-(Year) (#), e.g., H2-3 for DH 12-02-10 3, H3-3 for DH12-03-10 3, and so on.

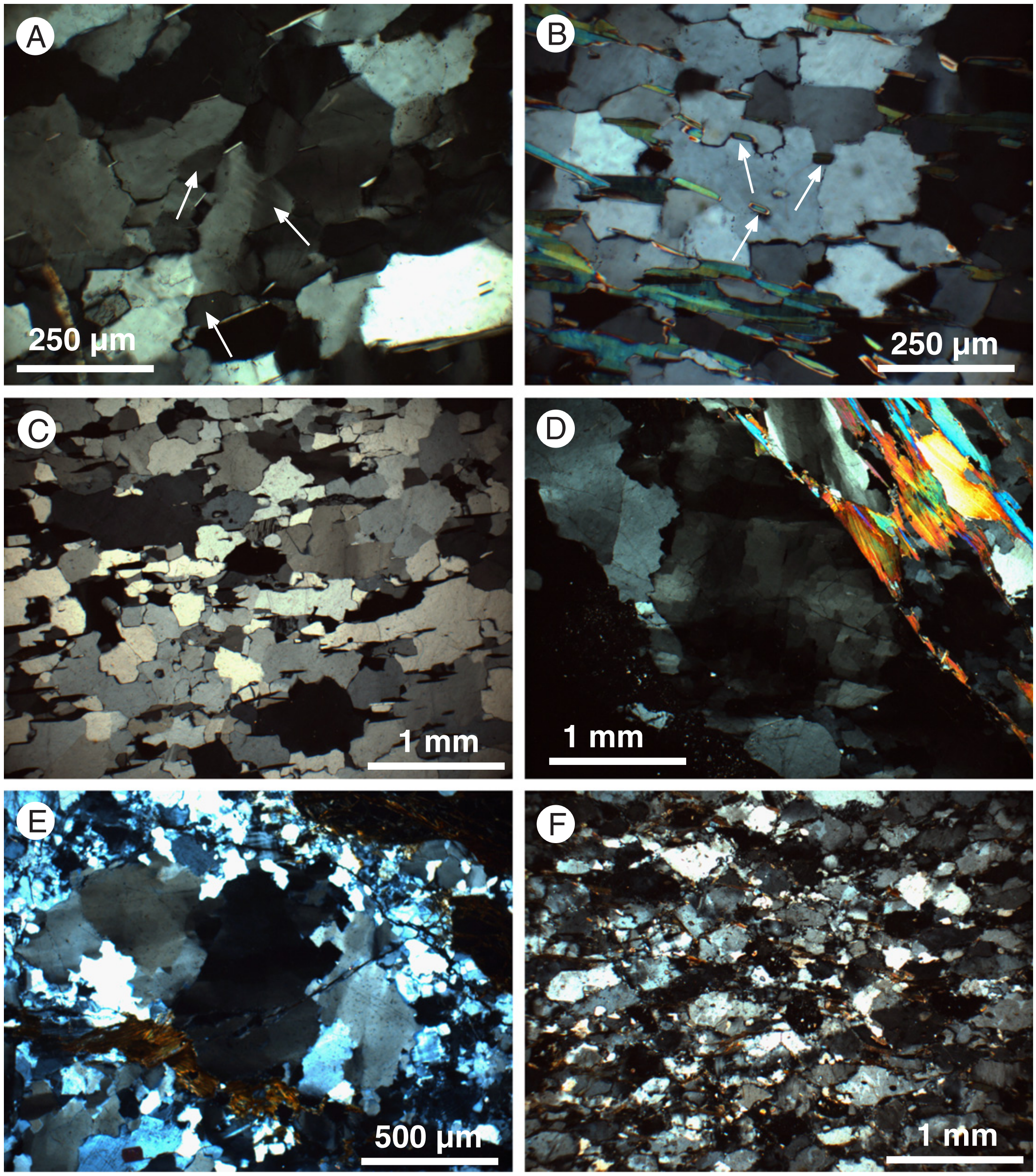

Fig. 8. Photomicrographs in cross-polarized light of representative samples from the Tila River transect showing quartz and feldspar deformation microstructures, arranged in an order of increasing structural positions. Locations of samples are marked in Fig. 6. (A) Sample H2-3 (MCT footwall): subgrains (two arrows at center) show the same size with new recrystallized grains (an arrow at middle-lower). (B) Sample H3-5C (MCT shear zone): pinning structures (two arrows at middle-upper) and mica inclusion completely enclosed in quartz crystal (an arrow at middle-lower) that represents an initial stage of formation of pinning structures. (C) Sample H3-8B (MCT zone): recrystallized quartz showing inequigranular texture with relatively large grain sizes (compare with (A)) and lobate grain shapes in response to grain boundary migration. (D) Sample H4-7 (between MCT and Tila shear zone): quartz chessboard extinction due to increased grain boundary migration. (E) Sample H5-5 (Tila shear zone): Large recrystallized quartz (center) has amoeboid grain boundaries. (F) Sample H6-7 (Tila shear zone hanging wall): relicts of large old quartz grains surrounded by small new recrystallized grains that are formed by bulging recrystallization.

5.2. Results

Samples H2-3 and H3-3 are from the MCT footwall (Fig. 6). Quartz *c*-axis fabrics of H2-3 define an asymmetric type-I cross-girdle pattern (Lister, 1977), indicating a top-to-the-south sense of shear. Sample H3-3 yields a symmetric type-II cross-girdle pattern (Fig. 9), which may be indicative of a pure shear component of deformation or a lack of simple shear (e.g., Larson et al., 2010a; Law et al., 2004).

Samples H3-5C, H3-8B, and H4-3 are from the MCT shear zone (Fig. 6). Sample H3-5C yields a weakly asymmetric type-I cross-girdle pattern that shows a top-to-the-south sense of shear (Fig. 9). The quartz *c*-axis fabric of sample H3-8B does not define a conventional cross-girdle pattern and the symmetry of the fabric cannot be used to determine a shear sense, however, a small circle girdle about the stereonet's lower pole may indicate a significant pure shear component of deformation (Fig. 9) (Schmid and Casey, 1986). A similar, though less well-developed small circle pattern may be present in sample H3-5C as well. Sample H4-3 yields a weakly asymmetric type-II cross-girdle pattern consistent with top-to-the-south shearing (Fig. 9). Where asymmetry exists, the samples from the MCT zone show top-to-the-south shearing, in agreement with field observations.

Samples H4-7 and H5-2 are from the section between the MCT and Tila shear zone (Fig. 6). Quartz *c*-axis fabrics from both samples define similar weakly asymmetric type-I cross-girdle patterns (Fig. 9), indicating a consistent top-to-the-south sense of shear.

Samples H5-5 and H5-12 are from the Tila shear zone (Fig. 6). They yield weakly asymmetric type-II cross-girdle fabrics (Fig. 9) (Lister, 1977), indicating a consistent top-to-the-north-northeast shear sense.

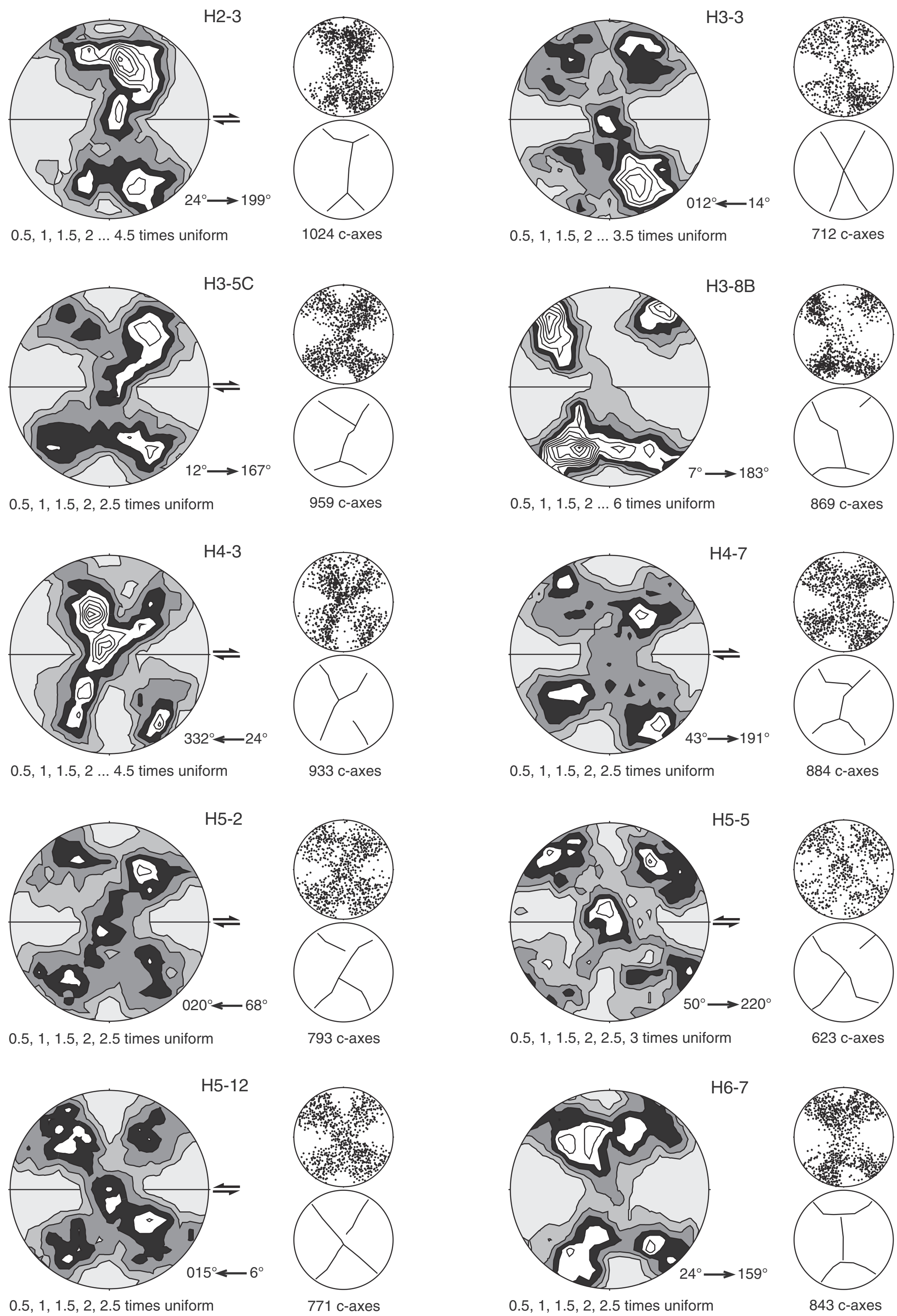

Fig. 9. Quartz *c*-axis fabric patterns of samples from the Tila River transect in the Dadeldhura klippe. All data are presented in lower hemisphere equal-area projection and viewed towards the east. The projection plane is perpendicular to foliation and parallel to lineation such that the lineation lies horizontal along in the E–W direction and the foliation plane lies vertical along the same direction. All quartz *c*-axis fabric plots are viewed towards the east such that, for example, a sinistral asymmetric pattern with respect to foliation indicates a top-to-the-north sense of shear. Relative shear sense with respect to foliation is indicated by half-arrows. Plunge and trend of lineations are presented by two numbers and an arrow. Samples are arranged in order of increasing structural positions from MCT footwall to Tila shear zone hanging wall. Sample locations are marked in Fig. 6.

Sample H6-7 is from the Tila shear zone hanging wall (Fig. 6). Quartz *c*-axis fabrics of this sample define a symmetric type-I cross-girdle pattern (Fig. 9). Weakly developed small circle girdles about the top and bottom poles of the stereonet may indicate a significant pure shear component to the deformation (Schmid and Casey, 1986).

5.3. Deformation temperatures by quartz c-axis fabrics

Assuming a consistent critical resolved shear stress and lack of hydrolytic weakening effects, the opening angles of quartz *c*-axis cross girdle fabrics may be used to make estimates of deformation temperature (Kruhl, 1998; Law et al., 2004; Lister and Hobbs, 1980; Tullis et al., 1973). Fabric opening angles have been empirically shown to have an approximately linear relationship between ~300 and 700 °C or approximately greenschist and amphibolite facies conditions (Fig. 10) (Kruhl, 1998; Law, 2014; Law et al., 2004). The rocks in the studied transect record greenschist to amphibolite facies conditions. Deformation temperatures derived through quartz *c*-axis fabrics are subject to an uncertainty of ±50 °C, which accounts for variation in the empirical correlation with metamorphic temperatures (and associated errors) and errors related to measurement uncertainty (Kruhl, 1998). Studies carried out across the Himalayan orogen indicate that deformation temperatures across both the MCT and STD estimated from fabric opening angles are comparable with the metamorphic temperatures derived from mineral composition and assemblage data (e.g., Law et al., 2004, 2011, 2013; Larson and Godin, 2009; Larson et al., 2010a, 2010b, 2013; Yakymchuk and Godin, 2012; see also review of Law, 2014). We therefore argue that the quartz *c*-axis fabric opening angle thermometer is applicable to our specimens and can be used to make reasonable deformation temperature estimates. These estimates are compared with metamorphic temperatures in the Discussion section.

In the MCT footwall, the opening angles of the quartz *c*-axis fabric girdles increase from 56° to 65° in samples H2-3 and H3-3, respectively. This corresponds to structural positions 600 (H2-3) and 200 m (H3-3) beneath the base of the MCT shear zone in Lesser Himalayan Sequence rocks. Within the MCT shear zone, three samples (H3-5C, H3-8B, and H4-3) yield quartz LPO opening angles of 76, 80, and 65°, corresponding to structural positions 100, 400, and 820 m above the base of the MCT shear zone, respectively. Between the MCT shear zone and the Tila shear zone, samples H4-7 and H5-2 are characterized by opening angles of 82–83° while, within the Tila shear zone, samples H5-5 and H5-12 yield opening angles from 82 to 75° with higher structural position. Finally, in the hanging wall of the Tila shear zone, sample H6-7 has a 61° fabric opening angle.

The samples (H2-3 and H3-3) in the MCT footwall indicate increasing deformation temperatures from 445 ± 50 to 520 ± 50 °C (compared to 450–550 °C from microstructures for both samples) with the increase of structural positions from 600 to 200 m below the base of the MCT (Fig. 10). The samples (H3-5C and H3-8B) from within the MCT shear zone record deformation temperatures of 605–635 ± 50 °C (compared

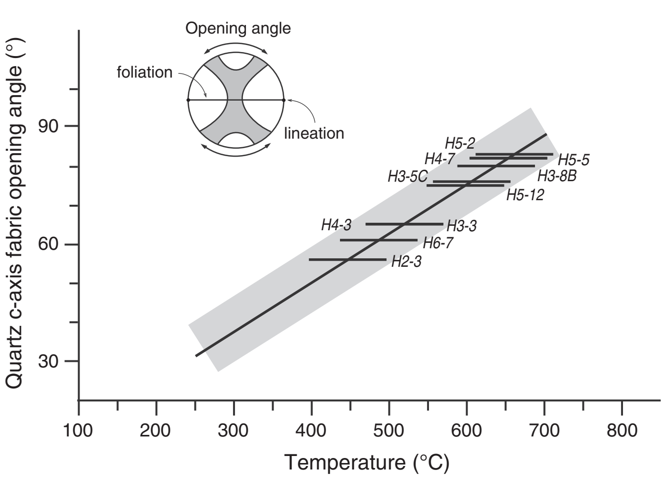

Fig. 10. Empirical relationship between opening angles of quartz *c*-axis fabric patterns and deformation temperatures with samples from the Tila River transect in the Dadeldhura klippe, modified from Law et al. (2004). Gray bar represents ±50 °C uncertainty. A conceptual *c*-axis fabric girdle on stereonet is shown in the upper-left corner.

to 550–650 °C from microstructures for both samples) at the lower part of the section, with deformation temperature decreasing slightly to 520 ± 50 °C (H4-3) (compared to 550–650 °C from microstructures) at the upper part of the section. The opening angles of the samples (H4-7 and H5-2) in between the MCT and Tila shear zone document consistently high deformation temperatures of 655–660 ± 50 °C (compared to 600–780 °C from microstructures for sample H4-7 and 550–650 °C for H5-2). The samples (H5-5 and H5-12) in the Tila shear zone exhibit decreasing opening angles with higher structural position, indicating deformation temperatures of 655 ± 50 °C to 600 ± 50 °C (compared to 550–650 °C from microstructures for both samples). A deformation temperature of 485 ± 50 °C (compared to 350–450 °C from microstructures) is indicated by the opening angle of 61° for the sample (H6-7) in the Tila shear zone hanging wall, the structurally highest sample examined.

6. U–Pb zircon geochronology

Two leucogranite samples from Tila shear zone in the Dadeldhura klippe were analyzed. Sixty spot data from 33 zircon grains were acquired using the CAMECA *ims* 1270 ion microprobe at the University of California-Los Angeles (UCLA). The detailed analytical procedure is described by Schmitt et al. (2003). The analyses were undertaken using an 8–15 nA O^- primary beam with an ~15 μm diameter spot size, which generated a crater with ~1 μm depth. U–Pb ratios were determined using a calibration curve based on UO/U versus Pb/U from zircon standard AS3 with age of 1099.1 Ma (Paces and Miller, 1993), and adjusted using common Pb for the Late Cenozoic (Stacey and Kramers, 1975). Concentrations of U were calculated by comparison with zircon standard 91500 with a U concentration of 81.2 ppm (Wiedenbeck et al., 2004). Data reduction was accomplished by the in-house program ZIPS 3.0 developed by Chris Coath.

6.1. Results

Sample H5-4 is from a leucogranitic dike intruding the host rock at the base of the Tila shear zone in the Dadeldhura klippe (Fig. 6). The leucogranite crosscuts the foliation of the host rocks (Fig. 7E, F) indicating that the leucogranitic dike is post-kinematic. Of the 33 spots from 18 zircon grains for this sample (Fig. 11 and Table S1), four Proterozoic to late Paleozoic $^{238}U/^{206}Pb$ ages spanning from ca. 832 to 313 Ma are discordant. Most of the remaining 29 spots analyses comprise a largely concordant $^{238}U/^{206}Pb$ age cluster from ca. 33.8 to 17.2 Ma (Fig. 11B). The Cenozoic ages consist of core ages of ca. 33.8–18.5 Ma and rim ages of ca. 23.9–17.2 Ma. The Paleozoic ages correspond to low-U concentrations (767–1224 ppm) and low U/Th ratios (3.4–41.4), whereas the Cenozoic ages correspond to high-U (>2000 ppm) and high U/Th ratios (>70). Cathodoluminescence (CL) images show that the Paleozoic ages only occur in the cores with bright, oscillatory-zoned cores, which are truncated by dark, concentrically zoned rims (Fig. 11A). The cores with Cenozoic ages are CL-bright or display mosaic textures, whereas rims display concentric zoning or convoluted zoning.

Sample H5-11B is from leucogranite intruding at the upper level of the Tila shear zone (Fig. 6). The leucogranite crosscuts foliation of the host rock and is undeformed (Fig. S1F, G), representing a post-kinematic intrusion. Twenty-seven spots from 15 zircon grains yield no pre-Cenozoic ages (Fig. 11B and Table S1). All $^{238}U/^{206}Pb$ ages are concordant and concentrate in the range from ca. 24.6 to 17.6 Ma with a single age at 14.3 Ma (Fig. 11B). Among these ages, the core analyses yield ca. 24.6-18.0 Ma while the rim ages spread from ca. 20.5 to 14.3 Ma. All ages correspond to high-U concentration (>2000 ppm) and high U/Th ratios (mostly >70). CL images reveal that these zircon grains are characterized by mosaic textures, overgrown by thin rims with convoluted zoning (Fig. 11A).

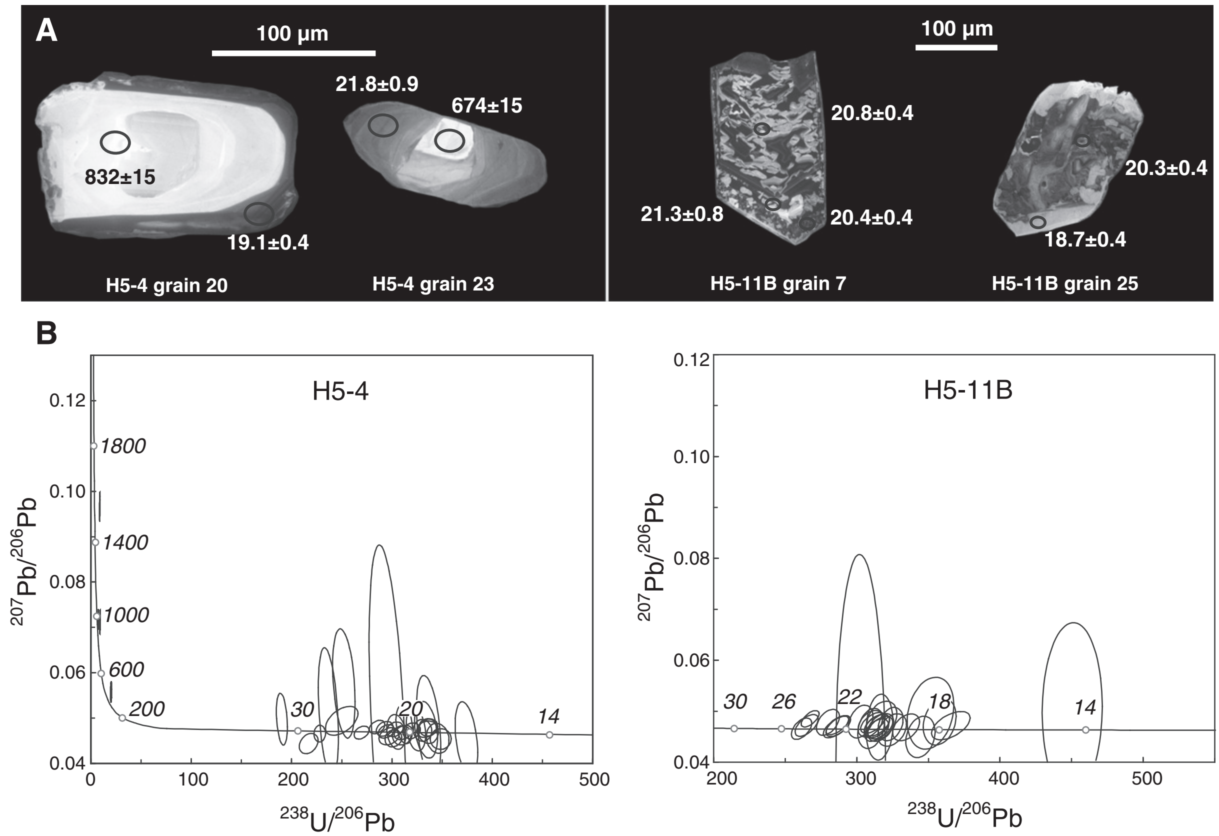

Fig. 11. U–Pb zircon geochronology of leucogranite samples from the Tila shear zone in the Dadeldhura klippe. (A) SEM cathodoluminescence (CL) images of representative zircon grains from two dated samples with $^{206}Pb/^{238}U$ ages. Spots are indicated by circles. (B) Concordia diagram of U–Pb analyses for leucogranites. Sample locations are marked in Fig. 6.

6.2. Interpretation

Cenozoic ages yield wide-ranged clusters for both samples, and mostly correspond to high U/Th ratios, which commonly indicate that zircon growth is related to metamorphic or hydrothermal events (e.g., Hoskin and Black, 2000; Rubatto, 2002; Rubatto et al., 2006). Both samples have some zircon grains that show mosaic textures in cores and convoluted zoning in rims. Mosaic textures may be developed by metasomatic replacement of zircon or represent metamict or recrystallized zircon grains (Corfu et al., 2003; Rubatto et al., 2012), while convoluted zoning may result from late to post-magmatic recrystallization of trace-element-rich domains or later metamorphic events (Corfu et al., 2003). The spread in Cenozoic age, which may indicate significant inherited material in such small dykes (Figs. 7E and S1F), may be exacerbated by an analytical matrix-effect associated with U–Pb analyses of high U, metamict zircon (e.g., White and Ireland, 2012; White et al., 2011). Correlation between age and U ppm is weak to non-existent in the two specimens (Fig. S3); excluding analyses with highest U concentrations would only slightly narrow the span of the Cenozoic ages (by ~2 myrs). The cores with pre-Cenozoic discordant ages in two samples are interpreted as inherited material. Below we only use the Cenozoic ages, which represent Himalayan events, for interpretations.

Sample H5-4, a post-kinematic intrusion with respect to the motion of the Tila shear zone, records core ages of ca. 33.8–18.5 Ma and rim ages of ca. 23.9–17.2 Ma (Fig. 11 and Table S1). Sample H5-11B, a post-kinematic intrusion with respect to the motion of the Tila shear zone, records core ages of ca. 24.6–18.0 Ma and rim ages of ca. 20.5–14.3 Ma (Fig. 11 and Table S1). Because of the potential for inherited zircon and matrix-effect associated with high U concentrations/metamictization, the data can only constrain the timing of youngest movement across the Tila shear zone. The youngest zircon rim ages extracted, ~17–14 Ma, provide a tentative youngest age limit on Tila shear zone activity.

7. Discussion

This study documents the presence of a top-to-the-north shear zone, termed as the Tila shear zone, along the northern margin of the Dadeldhura klippe. It separates a slice of high-grade kyanite-bearing rocks to the north from the medium- to low-grade metasedimentary rocks to the south. The Tila shear zone occurs ~3 km structurally above the MCT shear zone across the northern portion of our study area; this structural separation thins to ~1 km in the southern portion of the study area (Fig. 6). Deformation temperatures estimated from quartz and feldspar microstructures and quartz *c*-axis fabrics show that an inverted metamorphic field gradient characterizes the section across the MCT shear zone and a right-way-up metamorphic field gradient characterizes the section across the Tila shear zone up-section (Fig. 12). The thermal gradient across the Tila shear zone is ~77–189 °C/km ((650 ± 50–450 ± 50) °C/1.5 ± 0.5 km, in which 650 ± 50 and 450 ± 50 °C are the average temperatures at the base of the Tila shear zone and the structurally-highest sampled locality approximately 800 m above the top of the Tila shear zone, respectively, and 1.5 ± 0.5 km is the structural distance between the two points where the temperatures are estimated). U–Pb zircon dating of post-kinematic leucogranites suggests that activity along the Tila shear zone ceased prior to ~17–14 Ma. Below, we discuss regional structural interpretations, primarily focusing on the likelihood that the Tila shear zone represents a southern branch of the STD and the implications of that interpretation.

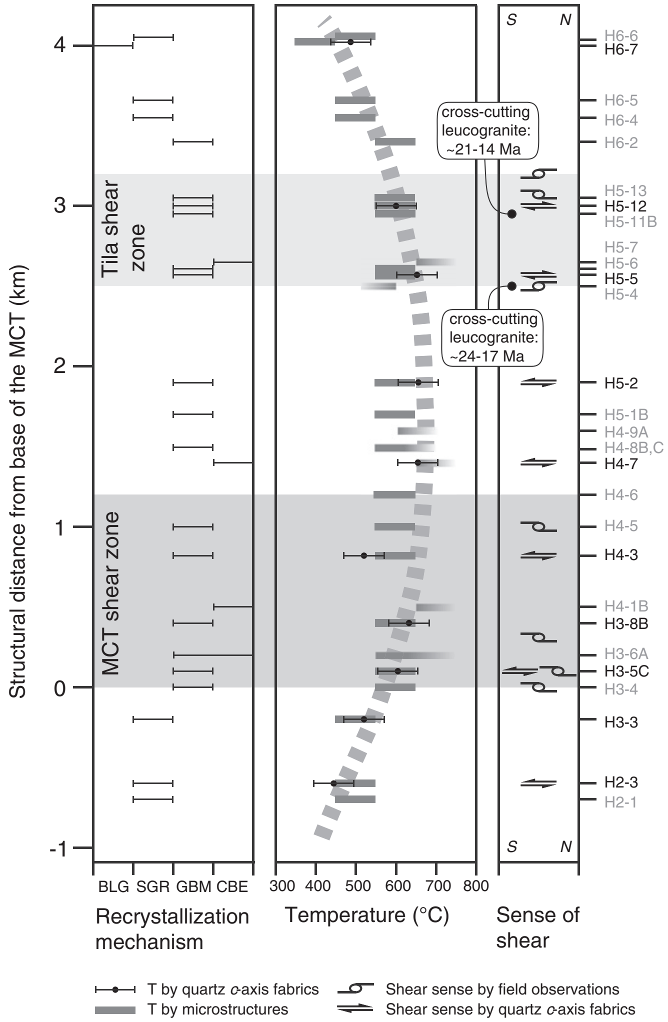

Fig. 12. Compilation of recrystallization mechanism, deformation temperature, and shear sense in a synthetic structural section for samples from the Tila River transect in the Dadeldhura klippe. Left column shows recrystallization mechanisms; middle column shows temperature ranges estimated from quartz microstructures (after Law, 2014 and Larson and Cottle, 2014) and temperatures with ±50 °C error bar estimated from opening angles of quartz *c*-axis fabric patterns (after Law et al., 2004). Right column shows shear sense obtained from field observations and quartz *c*-axis fabrics. The light gray filled box represents the Tila shear zone, and the dark gray filled box represents the MCT shear zone. Bold dashed curve in the middle column shows a trend of temperatures versus structural positions. Samples listed on the right are all samples in the paper for analytical work; samples in black are those conducted quartz *c*-axis fabric analysis. U–Pb ages of two leucogranite samples from the Tila shear zone are also shown in the right column. BLG — bulging; SGR — subgrain rotation; GBM — grain boundary migration; CBE — chessboard extinction.

7.1. Structural interpretations along the Tila River transect

7.1.1. The Jumla anticline

Within the Dadeldhura klippe, we interpret a km-scale fold structure, named the Jumla anticline, in the MCT hanging wall. This interpretation is primarily based on the systematic variation of the foliation orientations across the southwestern half of the study area (Fig. 6). The foliation here changes up-section from gentle SW dips in the MCT shear zone, to steep dips (both SW and NE) between the MCT and Tila shear zones, to uniformly N dips in the Tila shear zone. Foliations in the Tila shear zone hanging wall progressively change from steep to gentle SWS-dipping orientations. As best illustrated in the cross section (Fig. 6B), we explain this dip variation within the context of a detachment fold along the MCT shear zone. We root this deformation along the MCT because our new observations and regional work (e.g., Antolin et al., 2013; Robinson et al., 2006) indicate that rocks within and beneath the MCT shear zone are not folded in this manner. We did not observe significantly different structural geometries in this region that could accommodate the constraints from foliation orientations. A fault-propagation fold geometry would be similar in overall shape, but we did not observe corresponding brittle fabrics that cut across the foliations. Detachment folds of similar shape, scale, and vergence have been observed along the MCT shear zone elsewhere in the range: e.g., the Phojal anticline (Epard et al., 1995; Frank et al., 1973, 1995; Webb et al., 2007). We also note that meter-scale folds occur in the immediate Tila shear zone footwall (Fig. 7G–H), consistent with the proposed hinge zone of the Jumla anticline. The meter-scale folds may represent parasitic folding within the interpreted larger structure.

7.1.2. The Tila shear zone = STD interpretation

We interpret the Tila shear zone as the southern extension of the STD because of the following similarities between the two shear zones: (1) Both the Tila shear zone and STD record primarily top-to-the-north shearing. (2) The high thermal gradient of ~77–189 °C/km across the Tila shear zone matches the thermal gradient across many STD exposures along the range (e.g., Cottle et al., 2011; Law et al., 2004, 2011). (3) Rocks between the MCT and Tila shear zone consist of a succession of paragneiss at lower level and calc-silicate with thin orthogneiss interlayers at higher level, which is characteristic of the Greater Himalayan Crystalline complex sections in the adjacent Annapurna region (e.g., Carosi et al., 2010; Corrie and Kohn, 2011; Hodges et al., 1996; Le Fort, 1975; Searle and Godin, 2003; Vannay and Hodges, 1996). (4) Rocks in the hanging wall of the Tila shear zone are metasedimentary rocks intruded by Cambrian–Ordovician granite, consistent with the lithological characteristics of the Proterozoic–Cambrian metasedimentary rocks of the Bhimphedi Group (e.g., DeCelles et al., 1998; Gehrels et al., 2006a, 2006b; Stöcklin, 1980; Upreti and Le Fort, 1999; Webb et al., 2011b). (5) Meter-scale north-vergent recumbent folds and upright folds in the rocks of the Tila shear zone hanging wall (also see Robinson et al., 2006) are similar to the folding structures in the Tethyan Himalayan Sequence structurally above the STD (e.g., Godin et al., 2011; Kellett and Godin, 2009; Searle, 2010). (6) The metamorphic pattern of an inverted metamorphic field gradient across the MCT and a right-way-up metamorphic field gradient across the Tila shear zone matches the classical metamorphic pattern across the MCT and STD, and in particular the Tila shear zone is closely coincident with the right-way-up kyanite isograd and a deformation temperature decrease from ~650 to ~550 °C (Fig. 12), which match the metamorphic pattern associated with the STD shear zone (e.g., Burchfiel et al., 1992; Chambers et al., 2009; Cottle et al., 2011; Jessup et al., 2008; Kellett et al., 2009; Vannay and Grasemann, 1998). (7) The distribution of U–Pb zircon ages from Tila shear zone leucogranite samples is consistent with STD timing constraints indicative of Early and Middle Miocene shearing (e.g., see summary by Godin et al., 2006).

We do not favor alternative interpretations for the Tila shear zone because of inconsistency with existing data. One alternative interpretation is that the Tila shear zone is a post-MCT structure associated with the formation of the Dadeldhura synform, which was passively folded by the growth of the underlying Lesser Himalayan duplex (e.g., Robinson et al., 2003, 2006). Therefore, the top-to-the-north shearing along the Tila shear zone is a product of flexural slip accompanying the Lesser Himalayan duplex development (e.g., Sapkota and Sanislav, 2013). However, our U–Pb zircon dating suggests that motion along the Tila shear zone ceased before ~17–14 Ma, whereas the Lesser Himalayan duplexing began at ~7–8 Ma (e.g., Robinson et al., 2003, 2006). Another interpretation is that the Tila shear zone is an early Paleozoic structure, similar to structures documented in the Kathmandu Nappe (Gehrels et al., 2003, 2006a). This model requires that the Tila shear zone occurs within a south-verging thrust belt of early Paleozoic age. However, the shear records are primarily top-to-the-north and the U–Pb zircon core and rim ages indicate protracted high temperatures (at and above shearing temperatures from Tila shear zone quartz microstructures) during the mid-Cenozoic.

The remainder of the Discussion largely incorporates the interpretation that the Tila shear zone is the southern continuation of the STD. We discuss several related issues in the context of the Himalayan tectonic evolution.

7.2. Structural geometry of the Dadeldhura Klippe

Different models predict that the lower ~5–10 km of the northeastern Dadeldhura Klippe contains only Greater Himalayan Crystalline complex rocks (Fig. 5A, B), a top-to-the-south thrust zone that is either the MCT (Fig. 5C) or an intra-Greater Himalayan Crystalline complex thrust (Fig. 5E), or a top-to-the-north STD backthrust (Fig. 5D). Our mapping documents the Tila shear zone here. If the Tila shear zone is the STD (see above), it follows from the widely recognized fault-based definition (see Section 2) that the basal fault of the Dadeldhura Klippe is the MCT, the high-grade rocks between the MCT and Tila shear zone are part of the Greater Himalayan Crystalline complex, and the Tila shear zone hanging wall rocks are part of the Tethyan Himalayan Sequence.

The structural geology along the mapped transect indicates that the Tila shear zone becomes closer to the MCT from north to south. Our cross section shows that in the north these faults are separated by ~3 km of structural section, whereas in the (buried) south these faults are ~1 km apart (Fig. 6B). This north-to-south increasing proximity is consistent with a broader regional pattern of STD–MCT southwards-increasing proximity. Approximately ~75 km north of the mapped transect, these faults are structurally separated by >15 km (Murphy and Copeland, 2005); nearby sections at lesser distances towards the hinterland record a monotonic decrease in separation (Fig. 13, section locations shown in Fig. 4) (e.g., Carosi et al., 2010; Hodges et al., 1996; Searle and Godin, 2003; Vannay and Hodges, 1996). The mapping of Antolin et al. (2013), at a slightly more foreland-ward position ~120 km west of our transect, shows the faults separated by only ~0.8 km along the northern margin of the Dadeldhura Klippe (Figs. 4 and 13).

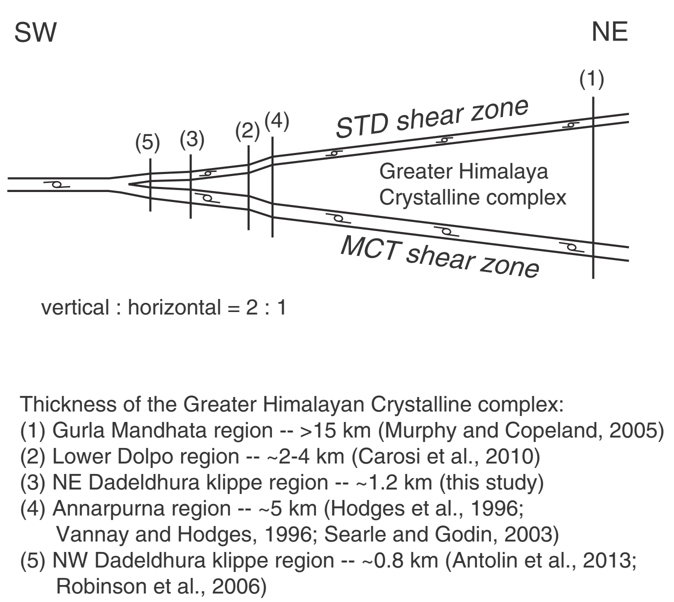

Fig. 13. Thinning of the Greater Himalayan Crystalline complex from north to south in central and western Nepal. Locations of five profiles are marked in Fig. 4. The structural thickness of the Greater Himalayan Crystalline complex at the five localities is projected into a common cross section that parallels the shortening direction (trending N30°E). It shows that the STD and MCT converge each other along the shortening direction from hinterland towards the foreland.

Antolin et al. (2013) identify the STD along the northern margin of the Dadeldhura Klippe along their transect via three criteria: (1) S–C–C′ shear fabrics showing top-to-the-north shearing, (2) Ar–Ar cooling ages indicating that the mapped shear zone ceased motion by 17 Ma, and (3) deformation temperatures of 400–500 °C within and above the shear zone, and 500–650 °C below the shear zone. On the southern flank of the synformal Dadeldhura Klippe, they interpret a contact ~10 km above the MCT as the STD. At present, structural evidence for deformation along this contact is limited to a single C′ shear band consistent with top-to-the-north shearing.

Antolin et al.'s model for the regional structural geometry (Fig. 5B; also see Figs. 1c and 8a of Antolin et al., 2013) shows that the thickness of the crystalline core decreases southwards to just ~4 km (inclusive of MCT and STD shear zone thickness) along the northern limb of the Dadeldhura Klippe synform, then increases farther south to ~11 km along the southern limb of the synform. Although the MCT and STD shear zones come within 1 km of merging in this model, the southwards divergence of these faults permits an STD normal fault interpretation. We do not favor this interpretation because of the currently restricted evidence for their proposed STD in the southern Dadeldhura Klippe. Instead, we extrapolate via the well-established relative MCT and STD positions (Figs. 4 and 13) and interpret an MCT-STD branch line (i.e., intersection) along the buried base of the Dadeldhura Klippe. Our interpretation is consistent with an STD backthrust model.

7.3. Interpolation of the MCT–STD branch line

Field evidence for the MCT–STD branch line has been presented along the arc of the orogen, but exposure of the branch line itself has not been documented (Webb et al., 2007, 2011a, 2011b, 2013; He et al., 2015; this study). Discussion with much of the Himalayan tectonics community reveals that this lack of documented branch line exposure is considered a signal problem, indicative of likely model failure. Here, we explain (1) why the branch line is unlikely to ever be observed directly, and (2) how interpolation demonstrates the existence of the branch line.

If the branch line exists, it is curvilinear — the intersection of the MCT and STD fault surfaces. For almost the entire length of the Himalayan orogen, this line would be either eroded or buried (as shown in Fig. 2). It would only be in the few spots that the posited branch line intersects the surface, across the southern portions of the Himalaya, that it could be exposed. Given the thicknesses of the fault zones, most of these spots could cover an area as large as a few hundred square meters to ~1 km^2. Because the southern Himalaya has limited access (largely restricted to rivers, and river-valley roads) and poor exposure (sparse road-cuts and stream-eroded bedrock exposures), the likelihood of such spots being both accessible and exposed is vanishingly small. Therefore, *even if the branch line interpretation is correct*, it is very unlikely that any worker will be able to map the branch line *directly*. The closest opportunity may be immediately west of the Galchi section along the northwestern Kathmandu Nappe, where the MCT and interpreted STD are separated by only a few hundred meters (He et al., 2015; Webb et al., 2011b). However, the Galchi section represents abnormally excellent exposure due to erosion along a local river; rocks in areas immediately west are both difficult to access (steep jungle terrain) and severely degraded by weathering.

Interpretation of the branch line via interpolation consists of a pair of extrapolations: (1) from the north, where both the MCT and STD can be traced, and (2) from the south, where no major structure separates the MCT from the Tethyan-correlative Phulchauki Group. The present work gives an example of the first extrapolation; as noted previously, regional constraints compellingly document southwards-increasing proximity of the MCT and STD (Fig. 13). The second extrapolation seems a contradiction in terms: along most studied sections the MCT is separated from

Tethyan rocks by the Greater Himalayan Crystalline complex and the STD. However, across the southern central Himalaya numerous field mapping projects have yielded scant evidence consistent with a major structure in the Bhimphedi-Phulchauki succession (e.g., DeCelles et al., 2001; Gehrels et al., 2006a, 2006b; Hayashi et al., 1984; Johnson et al., 2001; Robinson et al., 2006; Stöcklin and Bhattarai, 1982). In short, from the crest of the Himalaya towards the south, the MCT and STD are observed to get closer to one another, whereas from the front of the range towards the north, the MCT hanging wall does not appear divided by any major structure. Termination of the STD between the domains of these two patterns is the simplest interpretation. Approaching the southern limit of the northern pattern, the STD shear zone is both ≤1 km structurally above the MCT shear zone and ≫100 m thick (Webb et al., 2011b; Antolin et al., 2013; He et al., 2015; this study). Diffuse termination of the STD is difficult to envision in this circumstance (e.g., Long and McQuarrie, 2010; Vannay et al., 2004; Wyss et al., 1999).

7.4. Viability of a STD backthrust model

For the STD backthrust model to be viable, it must be able to explain evidence heretofore taken as clear proof of STD normal faulting and it must be consistent with the general geology of the Himalayan orogen. The most basic data long taken as proof of STD normal faulting are the top-to-the-north, north-dipping STD exposures that juxtapose lower grade rocks atop higher grade rocks along the Himalayan range crest (e.g., Burchfiel et al., 1992). However, rich literature shows that the STD is folded, exposed in various locations along an across-strike distance of ~200 km (e.g., Chen et al., 1990; Grujic et al., 2002; Wagner et al., 2010; and this study — see the "Orogenic framework" section above). Along this ~200 km span in the transport direction, (1) the change in STD exposure elevation cannot exceed Everest's 8850 m peak, (2) the STD displays no change in characteristic thermal gradient (see the "Orogenic framework" section above), and (3) the STD does not have a fault-correlated offset in thermochronological ages (see data compilations of Yin, 2006 and Martin et al., 2014). Therefore basic dip, shear, thermal, and thermochronometric patterns commonly assumed to support top-to-the-north normal faulting instead indicate that the STD is flat at first-order. The thermal data consistency from N to S shows that it was sub-horizontal during motion, and the current geometry shows that it is sub-horizontal now.

Additional features understood as evidence for STD normal faulting include flattening of section, excision of section, and the presence of brittle faults along the STD shear zone (e.g., Law et al., 2004, 2011; Long et al., 2011; Corrie et al., 2012; N. McQuarrie, 2013, pers. comm.). Flattening is recognized on the basis of general shear kinematics within the STD shear zone. However, this does not inform the orogen-scale kinematics of the shear zone, i.e., flattening does not dictate whether the shear zone accomplishes large-scale extension or contraction. As an illustrative comparison, note that the MCT preserves similar general shear/flattening characteristics and is clearly recognized as a major contractional feature (e.g., Grasemann et al., 1999). Similarly, observations of section excision do not require extension. Section excision may not reflect deformation, but may instead result from regional stratigraphic variations (see the "Orogenic framework" section above). Furthermore, the apparent section excision shows the immediate STD hanging wall getting younger to the north; if this does represent structural excision then it is consistent with top-to-the-north thrusting, not top-to-the-north normal faulting (e.g., Yin et al., 2010). Brittle faults are missing at many STD exposures (see the "Orogenic framework" section above) and difficult to uniquely ascribe to STD motion (see discussion in Webb et al., 2013). One signal exception is the brittle STD exposed in the Everest–Rongbuk area, which we discuss below.

Local development of Riedel shears may explain the limited spatial extent of apparent brittle detachments along the STD. Namely, if late concentrated STD shearing was locally focused along shear-zone-scale Riedel shears, local excision of portions of the broad STD shear zone may have resulted (see Fig. 14 for further explication). Despite such local excision, at orogenic scale the fault could remain sub-horizontal throughout its entire motion history. Therefore this kinematic evolution is equally compatible with large-scale contraction and extension. This Riedel shear concept may be relevant in the Everest region. There, a brittle fault is well developed at the top of the STD shear zone and has an associated ~100–150 °C thermal break (Corthouts and Lageson, 2013; Searle et al., 2003), whereas just ~35 km to the east the STD occurs as a shear zone with a continuous, condensed metamorphic field gradient from footwall to hanging wall (Cottle et al., 2011). The Everest STD may record local development of a Riedel shear segment during late STD motion, whereas local late motion ~35 km to the east may have remained sub-parallel to older shear zone boundaries.

In summary, evidence along the length and breadth of the STD does not require normal faulting or thrust faulting, but rather that the STD was active as a sub-horizontal shear zone. In general terms, this structure may be consistent with our understanding of backthrusts: sub-horizontal backthrusts are common structures in fold-thrust belts (e.g., Jones, 1982; Lawton et al., 1994; Price, 1986) and the architecture and kinematics of a wedge bounded by a basal thrust and a roof backthrust are mechanically viable (e.g., Erickson, 1995; Jamison, 1996; Smart et al., 1999). Determination of whether a roughly flat shear zone is a normal or thrust fault requires knowledge of the

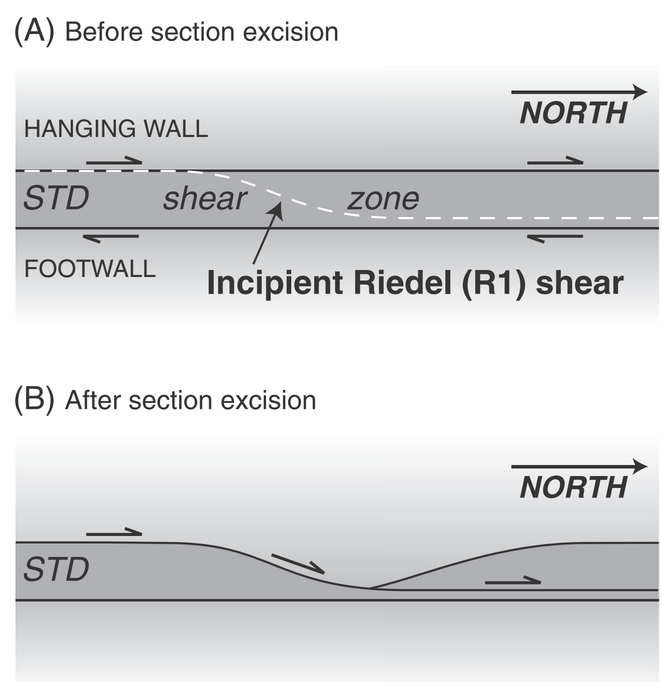

Fig. 14. Schematic kinematic evolution of the STD shear zone. The sketch highlights potential late-phase faulting – a concentrated shear zone/brittle fault — within the developed STD shear zone. The late-phase faulting locally propagates as a shear-zone scale Riedel (R1) shear. This is similar to the argument of Yin and Taylor (2011), who suggest that low-angle normal faults may represent crustal-scale and/or upper-crustal-scale Riedel shears. In this case, the Riedel shear is limited to the shear zone and represents a continuation of main fault motion. In the backthrust fault interpretation of this subhorizontal structure, the shear-zone scale Riedel shear represents a thrusting fabric in the same way that S–C fabric does. In this example, the Riedel geometry of late-phase faulting leads to local excision of the upper portions of the STD shear zone. (A) Before section excision, the STD shear zone boundaries are roughly parallel and sub-horizontal. As orogenesis and corresponding exhumation of the wedge above the Himalayan sole thrust continue, deformation becomes increasingly concentrated into brittle structures, which could include Riedel shears as shown . (B) After late shearing and development of a Riedel shear, the thickness of the STD shear zone varies along the transport direction. The upper portion of the STD shear zone is locally excised immediately above the footwall portion of the Riedel shear segment of the late fault. Note that despite local variations, at orogenic scale the STD is subhorizontal throughout its entire deformation. This may be consistent with either contractional or extensional deformation.

terminations of the shear zone. In this case, we return to our identification of an STD root zone along the southern Himalaya as the deciding factor confirming the STD backthrust interpretation. To the north, STD backthrust slip may have been transferred to hanging wall north-vergent fold-thrust systems (e.g., Godin et al., 1999; Steck et al., 1999) and/or the Great Counter thrust (Yin, 2006).

7.5. Does the STD record alternation of top-north and top-south shearing during main motion?

The STD has been interpreted as an alternating top-to-the-south and top-to-the-north shear zone because it locally contains a mix of the top-to-the-north and top-to-the-south shear structures (e.g., Godin et al., 1999; Hodges et al., 1996; Mukherjee and Koyi, 2010; Webb et al., 2007). An alternation of shear sense would impose a powerful constraint on STD tectonic models. However, the preserved fabrics allow that key indicators for shear-sense alternation may pre- and post-date the main activity on the shear zone, such that the main motion of the shear zone was exclusively top-to-the-north. We consider "main motion" to represent the period when the STD was active as a major shear zone operating within the orogenic wedge, and the MCT (or MCT-II) was active as the sole thrust of the orogen, i.e., the period represented in the Himalayan constructional models of Fig. 1. Before this period, the STD may have been active as the base of the Tethyan Himalayan fold-thrust belt, and thus developed top-south shear sense indicators (e.g., Aikman et al., 2008; Godin et al., 1999; Kellett and Godin, 2009; Murphy and Yin, 2003; Ratschbacher et al., 1994; Vannay and Steck, 1995; Wiesmayr and Grasemann, 2002; Yin et al., 1999). After this period, the STD may be periodically deformed in a top-to-the-north or top-to-the-south direction along with the bulk of the orogenic wedge via taper-building and -diminishing processes such as out-of-sequence faulting/folding and minor normal faulting (e.g., Steck et al., 1993; Vannay and Steck, 1995; Webb, 2013). Therefore, deformation prior to STD main motion could impart early top-to-the-south shear sense in the shear zone (also, top-to-the-south MCT shear indicators could be transferred to the STD shear zone during tectonic wedging, as explained in Webb et al., 2007). Low-magnitude deformation after main motion could create both top-to-the-north and top-to-the-south structures. Observed examples of such late structures commonly cross-cut the STD, e.g., low-slip (~<5 km) normal faults (e.g., Steck et al., 1993; Vannay and Steck, 1995).

These considerations suggest that early top-to-the-south, dominant top-to-the-north, and late mixed-mode deformation could be commonly recorded across the STD without necessitating alternating shearing during main STD motion. Indeed, this is the dominant deformation pattern recorded along the STD (e.g., Godin et al., 1999; Hodges et al., 1996; Mukherjee and Koyi, 2010; Webb et al., 2007).

A key question remains: what record could suggest alternating shear along the STD during main motion? Such a record should display two periods of dominantly top-to-the-north STD shearing separated by a top-to-the-south shearing period, with all shearing along the shear zone (i.e., not cross-cutting the shear zone). Such a record has only been reported by Hodges et al. (1996), who interpret top-to-the-south shear records as intervening between two top-to-the-north shearing episodes along the STD in the Annapurna, ~150 km to the east of our study area. However, the top-to-the-south shear structures reported by Hodges et al. can alternatively be interpreted to precede all top-to-the-north shear records. Therefore, there is no known evidence that exclusively requires alternating shearing during main STD motion.

Eliminating the requirement of alternating STD main motion allows modification of the tectonic wedging model of Webb et al. (2007). The original model requires a second northern tectonic wedge in the hinterland to feed slip into the STD backthrust system, such that the sub-horizontal STD may be periodically modified from a top-to-the-north backthrust to a top-to-the-south thrust (see Fig. 4H of Webb et al., 2007). The revised modified model, featuring exclusively top-to-the-north backthrusting during STD main motion, does not require this second tectonic wedge (Fig. 1C).

8. Conclusions

New field mapping and kinematic analysis demonstrate that a primarily top-to-the-north shear zone, termed as the Tila shear zone, occurs in the Dadeldhura klippe of western Nepal. The Tila shear zone is correlated to the STD on the bases of lithologic, metamorphic, and kinematic consistency. Thus, the Greater Himalayan Crystalline complex displays a wedge shape tapering to the south, and the Tila shear zone/STD potentially merges with the MCT at depth along the Dadeldhura klippe. This work serves as the most richly detailed description of such an STD–MCT merger to date, bolstering similar prior interpretations along the Himalayan range (e.g., Kellett and Grujic, 2012; Leger et al., 2013; Webb et al., 2007, 2011a, 2011b; Yin, 2006). These findings – in particular the orogen-scale structural geometry and kinematic history – require that (1) the STD moved as a crustal-scale backthrust rather than as a normal fault, and (2) the Greater Himalayan Crystalline complex was emplaced at depth via tectonic wedging.

This distinctive interpretation of the STD serves as a critical criterion to differentiate extrusion and duplexing models for the emplacement of the Himalayan crystalline core (the Greater Himalayan Crystalline complex). Tectonic wedging is a duplexing model. The local preservation of the STD-backthrust root zone, which marks the leading edge of the Greater Himalayan Crystalline complex, requires that these rocks were not extruded to the surface during motion on the bounding faults. Recent work indicates that the development of the Greater Himalayan Crystalline complex (Corrie and Kohn, 2011; Larson and Cottle, 2014) and ongoing deformation of the Himalaya (Herman et al., 2010; Yu et al., 2015) are dominated by duplexing processes. We therefore speculate that Himalayan mountain-building has been dominated by duplexing since as early as Oligocene time, and develop this idea further in a companion work (see the companion paper of He et al., 2015).

Acknowledgments

This paper benefits from discussion with P. Clift, C. Colón, D. Donaldson, H. Guo, and H. Yu. An early draft has been significantly improved by reviews from D. Robinson, M. Rusmore, J.P. Burg, and L. Jolivet. We thank E. Burov for editorial handling as well as L. White and an anonymous reviewer for constructive feedback which led to significant improvement in communication. This work was supported by a GSA student research grant to Dian He and grants from Louisiana State University (start-up), the Louisiana Board of Regents (LEQSF (2012–15)-RD-A-12), and the Tectonics program of the U.S. National Science Foundation (EAR-1322033). We thank Bhim Chand and his colleagues at Earth's Paradise Treks and Adventures for field logistical support.

Appendix A. Supplementary data

Supplementary data to this article can be found online at http://dx.doi.org/10.1016/j.tecto.2015.11.014.

References

Aikman, A.B., Harrison, T.M., Lin, D., 2008. Evidence for Early (>44 Ma) Himalayan crustal thickening, Tethyan Himalaya, southeastern Tibet. Earth Planet. Sci. Lett. 274, 14–23.

Allmendinger, R.W., 2012. Stereonet 7.2.4. http://www.geo.cornell.edu/geology/faculty/RWA/programs/stereonet.html (accessed March 2012).

Antolin, B., Godin, L., Wemmer, K., Nagy, C., 2013. Kinematics of the Dadeldhura klippe shear zones (W Nepal): implications for the foreland evolution of the Himalayan metamorphic core. Terra Nova 25, 282–291.

Arita, K., 1983. Origin of the inverted metamorphism of the Lower Himalayas Central Nepal. Tectonophysics 95, 43–60.

Beaumont, C., Jamieson, R.A., Nguyen, M.H., Lee, B., 2001. Himalayan tectonics explained by extrusion of a low-viscosity crustal channel coupled to focused surface denudation. Nature 414, 738–742.

Bollinger, L., Avouac, J.P., Beyssac, O., Catlos, E.J., Harrison, T.M., Grove, M., Goffé, B., Sapkota, S., 2004. Thermal structure and exhumation history of the Lesser Himalaya in central Nepal. Tectonics 23, TC5015. http://dx.doi.org/10.1029/2003TC001564.
Brown, R.L., Gibson, H.D., 2006. An argument for channel flow in the southern Canadian Cordillera and comparison with Himalayan tectonics. In: Law, R., Searle, M.P., Godin, L. (Eds.), Channel Flow, Ductile Extrusion, and Exhumation in Continental Collision Zones. Geol. Soc. London Spec. Pub. 268, pp. 543–559.
Burchfiel, B.C., Royden, L.H., 1985. North–south extension within the convergent Himalayan region. Geology 13, 679–682.
Burchfiel, B.C., Chen, Z., Hodges, K.V., Liu, Y., Royden, L.H., Deng, C., Xu, J., 1992. The South Tibetan detachment system, Himalaya orogen: extension contemporaneous with and parallel to shortening in a collisional mountain belt. Geol. Soc. Am. Spec. Pap. 269, 1–41.
Burg, J.P., Brunel, M., Gapais, D., Chen, G.M., Liu, G.H., 1984. Deformation of leucogranites of the crystalline Main Central Sheet in southern Tibet (China). J. Struct. Geol. 6, 535–542.
Carosi, R., Lombardo, B., Molli, G., Musumeci, G., Pertusati, P.C., 1998. The South Tibetan detachment system in the Rongbuk valley, Everest region. Deformation features and geological implications. J. Asian Earth Sci. 16, 299–311.
Carosi, R., Montomoli, C., Visonà, D., 2007. A structural transect in the Lower Dolpo: insights on the tectonic evolution of Western Nepal. J. Asian Earth Sci. 29, 407–423.
Carosi, R., Montomoli, C., Rubatto, D., Visonà, D., 2010. Late Oligocene high-temperature shear zones in the core of the Higher Himalayan Crystallines (Lower Dolpo, western Nepal). Tectonics 29, TC4029. http://dx.doi.org/10.1029/2008TC002400.
Catlos, E.J., Harrison, T.M., Kohn, M.J., Grove, M., Ryerson, F.J., Manning, C.E., Upreti, B.N., 2001. Geochronologic and thermobarometric constraints on the evolution of the Main Central Thrust, central Nepal Himalaya. J. Geophys. Res. 106, 16177–16204.
Célérier, J., Harrison, T.M., Webb, A.A.G., Yin, A., 2009. The Kumaun and Garwhal Lesser Himalaya, India; part 1, structure and stratigraphy. Geol. Soc. Am. Bull. 121, 1262–1280.
Chambers, J., Caddick, M., Argles, T., Horstwood, M., Sherlock, S., Harris, N., Parrish, R., Ahmad, T., 2009. Empirical constraints on extrusion mechanisms from the upper margin of an exhumed high-grade orogenic core, Sutlej valley, NW India. Tectonophysics 477, 77–92.
Chen, Z., Liu, Y., Hodges, K.V., Burchfiel, B.C., Royden, L.H., Deng, C., 1990. The Kangmar dome: a metamorphic core complex in southern Xizang (Tibet). Science 250, 1552–1556.
Coleman, M.E., 1998. U–Pb constraints on Oligocene-Miocene deformation and anatexis within the central Himalaya, Marsyandi valley, Nepal. Am. J. Sci. 298, 553–571.
Cooper, F.J., Adams, B.A., Edwards, C.S., Hodges, K.V., 2012. Large normal-sense displacement on the South Tibetan fault system in the eastern Himalaya. Geology 40, 971–974.
Cooper, F.J., Hodges, K.V., Adams, B.A., 2013. Metamorphic constraints on the character and displacement of the South Tibetan fault system, central Bhutanese Himalaya. Lithosphere 5, 67–81.
Corfu, F., Hanchar, J.M., Hoskin, P.W.O., Kinny, P., 2003. Atlas of zircon textures. Rev. Mineral. Geochem. 53, 469–500.
Corrie, S.L., Kohn, M.J., 2011. Metamorphic history of the central Himalaya, Annapurna region, Nepal, and implications for tectonic models. Geol. Soc. Am. Bull. 123, 1863–1879.
Corrie, S.L., Kohn, M.J., McQuarrie, N., Long, S.P., 2012. Flattening the Bhutan Himalaya. Earth Planet. Sci. Lett. 349–350, 67–74.
Corthouts, T., Lageson, D.R., 2013. Petrography of the Ordovician Qomolangma Formation and Yellow Band, Mount Everest, Nepal. GSA Meeting Abstract (No. 255–10).
Cottle, J.M., Jessup, M.J., Newell, D.L., Searle, M.P., Law, R.D., Horstwood, M.S.A., 2007. Structural insights into the early stages of exhumation along an orogen-scale detachment: the South Tibetan Detachment System, Dzakaa Chu section, Eastern Himalaya. J. Struct. Geol. 29, 1781–1797.
Cottle, J.M., Watters, D.J., Riley, D., Beyssac, O., Jessup, M.J., 2011. Metamorphic history of the South Tibetan Detachment System, Mt. Everest region, revealed by RSCM thermometry and phase equilibria modeling. J. Metamorph. Geol. 29, 561–582.
Crouzet, C., Dunkl, I., Paudel, L., Árkai, P., Rainer, T.M., Balogh, K., Appel, E., 2007. Temperature and age constraints on the metamorphism of the Tethyan Himalaya in Central Nepal: a multidisciplinary approach. J. Asian Earth Sci. 30, 113–130.
Daniel, C.G., Hollister, L.S., Parrish, R.R., Grujic, D., 2003. Exhumation of the Main Central thrust from lower crustal depths, eastern Bhutan Himalaya. J. Metamorph. Geol. 21, 317–334.
DeCelles, P.G., Gehrels, G.E., Quade, J., Ojha, T.P., Kapp, P.A., Upreti, B.N., 1998. Neogene foreland basin deposits, erosional unroofing, and the kinematic history of the Himalayan fold-thrust belt, western Nepal. Geol. Soc. Am. Bull. 110, 2–21.
DeCelles, P.G., Gehrels, G.E., Quade, J., LaReau, B., Spurlin, M., 2000. Tectonic implications of U–Pb zircon ages of the Himalayan orogenic belt in Nepal. Science 288, 497–499.
DeCelles, P.G., Robinson, D.M., Quade, J., Ojha, T.P., Garzione, C.N., Copeland, P., Upreti, B.N., 2001. Stratigraphy, structure, and tectonic evolution of the Himalayan fold-thrust belt in western Nepal. Tectonics 20, 487–509.
DiPietro, J.A., Pogue, K.R., 2004. Tectonostratigraphic subdivisions of the Himalaya: a view from the west. Tectonics 23, TC5001. http://dx.doi.org/10.1029/2003TC001554.
Epard, J.L., Steck, A., Vannay, J.C., Hunziker, J., 1995. Tertiary Himalayan structures and metamorphism in the Kulu Valley (Mandi–Khoksar Transect of the Western Himalaya) — Shikar-Beh-Nappe and Crystalline Nappe. Schweiz. Mineral. Petrogr. Mitt. 75, 59–84.
Erickson, S.G., 1995. Mechanics of triangle zones and passive-roof duplexes: implications of finite-element models. Tectonophysics 245, 1–11.
Frank, W., Hoinkes, G., Miller, C., Purtscheller, F., Richter, W., Thoni, M., 1973. Relations between metamorphism and orogeny in a typical section of the Indian Himalayas. Tschermaks Mineral. Petrogr. Mitt. 20, 303–332.
Frank, W., Grasemann, B., Guntli, P., Miller, C., 1995. Geological Map of the Kishtwar–Chamba–Kulu Region (NW Himalayas, India). Jahrb. Geol. Bundesanst. 138, 299–308.
Fritz, H., Tenczer, V., Hauzenberger, C., Wallbrecher, E., Muhongo, S., 2009. Hot granulite nappes — tectonic styles and thermal evolution of the Proterozoic granulite belts in East Africa. Tectonophysics 477, 160–173.
Funakawa, S., 2001. Lower Paleozoic Tethys sediments from the Kathmandu Nappe, Phulchauki area, central Nepal. J. Nepal Geol. Soc. 25, 123–134.
Gansser, A., 1964. The Geology of the Himalayas. Wiley Interscience, New York (289 pp.).
Garzanti, E., 1999. Stratigraphy and sedimentary history of the Nepal Tethys Himalaya passive margin. J. Asian Earth Sci. 17, 805–827.
Gehrels, G.E., DeCelles, P.G., Martin, A., Ojha, T.P., Pinhassi, G., Upreti, B.N., 2003. Initiation of the Himalayan Orogen as an early Paleozoic thin-skinned thrust belt. GSA Today 13, 4–9.
Gehrels, G.E., DeCelles, P.G., Ojha, T.P., Upreti, B.N., 2006a. Geologic and U–Th–Pb geochronologic evidence for early Paleozoic tectonism in the Kathmandu thrust sheet, central Nepal Himalaya. Geol. Soc. Am. Bull. 118, 185–198.
Gehrels, G.E., DeCelles, P.G., Ojha, T.P., Upreti, B.N., 2006b. Geologic and U–Pb geochronologic evidence for early Paleozoic tectonism in the Dadeldhura thrust sheet, far-west Nepal Himalaya. J. Asian Earth Sci. 28, 385–408.
Giovanni, M.K., Horton, B.K., Garzione, C.N., McNulty, B., 2010. Extensional basin evolution in the Cordillera Blanca, Peru: stratigraphic and isotopic records of detachment faulting and orogenic collapse in the Andean hinterland. Tectonics 29, TC6007. http://dx.doi.org/10.1029/2010TC002666.
Girault, F., Perrier, F., Gajurel, A.P., Bhattarai, M., Koirala, B.P., Bollinger, L., Fort, M., France-Lanord, C., 2012. Effective radium concentration across the Main Central Thrust in the Nepal Himalayas. Geochim. Cosmochim. Acta 98, 203–227.
Godin, L., 2003. Structural evolution of the Tethyan sedimentary sequence in the Annapurna area, central Nepal Himalaya. J. Asian Earth Sci. 22, 307–328.
Godin, L., Brown, R.L., Hanmer, S., 1999. High strain zone in the hanging wall of the Annapurna detachment, central Nepal Himalaya. In: Macfarlane, A., Sorkhabi, R.B., Quade, J. (Eds.), Himalaya and Tibet: Mountain Roots to Mountain Tops. Geological Society of America, Special Papers 328, pp. 199–210.
Godin, L., Parrish, R.R., Brown, R.L., Hodges, K.V., 2001. Crustal thickening leading to exhumation of the Himalayan metamorphic core of central Nepal: insight from U–Pb geochronology and $^{40}Ar/^{39}Ar$ thermochronology. Tectonics 20, 729–747.
Godin, L., Grujic, D., Law, R., Searle, M.P., 2006. Crustal flow, extrusion, and exhumation in continental collision collision zones: an introduction. In: Law, R., Searle, M.P., Godin, L. (Eds.), Channel Flow, Ductile Extrusion, and Exhumation in Continental Collision Zones. Geol. Soc. London Spec. Pub. 268, pp. 1–23.
Godin, L., Yakymchuk, C., Harris, L.B., 2011. Himalayan hinterland-verging superstructure folds related to foreland-directed infrastructure ductile flow: insights from centrifuge analogue modeling. J. Struct. Geol. 33, 329–342.
Goscombe, B., Hand, M., 2000. Contrasting P–T paths in the Eastern Himalaya, Nepal: inverted isograds in a paired metamorphic mountain belt. J. Petrol. 41, 1673–1719.
Goscombe, B., Gray, D., Hand, M., 2006. Crustal architecture of the Himalayan metamorphic front in eastern Nepal. Gondwana Res. 10, 232–255.
Grasemann, B., Fritz, H., Vannay, J.-C., 1999. Quantitative kinematic flow analysis from the Main Central Thrust Zone (NW-Himalaya, India): implications for a decelerating strain path and the extrusion of orogenic wedges. J. Struct. Geol. 21, 837–853.
Grujic, D., Casey, M., Davidson, C., Hollister, L.S., Kündig, R., Pavlis, T., Schmid, S., 1996. Ductile extrusion of the Higher Himalayan crystallines in Bhutan: evidence from quartz microfabrics. Tectonophysics 260, 21–43.
Grujic, D., Hollister, L.S., Parrish, R.R., 2002. Himalayan metamorphic sequence as an orogenic channel: insight from Bhutan. Earth Planet. Sci. Lett. 198, 177–191.
Grujic, D., Warren, C.J., Wooden, J.L., 2011. Rapid synconvergent exhumation of Miocene-aged lower orogenic crust in the eastern Himalaya. Lithosphere 3, 346–366.
Hanmer, S., Williams, M., Kopf, C., 1995. Modest movements, spectacular fabrics in an intracontinental deep-crustal strike-slip fault: Striding-Athabasca mylonite zone, NW Canadian Shield. J. Struct. Geol. 17, 493–507.
Harrison, T.M., Ryerson, F.J., Le Fort, P., Yin, A., Lovera, O.M., Catlos, E.J., 1997. A Late Miocene–Pliocene origin for the Central Himalayan inverted metamorphism. Earth Planet. Sci. Lett. 146, 1–8.
Harrison, T.M., Grove, M., Lovera, O.M., Catlos, E.J., D'Andrea, J., 1999. The origin of Himalayan anatexis and inverted metamorphism: models and constraints. J. Asian Earth Sci. 17, 755–772.
Hayashi, D., Fujii, Y., Yoneshiro, T., Kizaki, K., 1984. Observations on the geology of the Karnali Region, West Nepal. J. Nepal Geol. Soc. 4, 29–40.
He, D., Webb, A.A.G., Larson, K.P., Martin, A.J., Schmitt, A.K., 2015. Extrusion vs. duplexing models of Himalayan mountain building 3: duplexing dominates from Oligocene to present. Int. Geol. Rev. 57, 1–27.
Heim, A., Gansser, A., 1939. Central Himalaya Geological Observations of Swiss Expedition 1936. Gebrüder Fretz, Zurich (246 pp.).
Herman, F., Copeland, P., Avouac, J.P., Bollinger, L., Maheo, G., Le Fort, P., Rai, S., Foster, D., Pecher, A., Stuwe, K., Henry, P., 2010. Exhumation, crustal deformation, and thermal structure of the Nepal Himalaya derived from the inversion of thermochronological and thermobarometric data and modeling of the topography. J. Geophys. Res. 115, B06407.
Herren, E., 1987. Zanskar shear zone: northeast–southwest extension within the Higher Himalaya. Geology 15, 409–413.
Hirth, G., Tullis, J., 1992. Dislocation creep regimes in quartz aggregates. J. Struct. Geol. 14, 145–159.
Hodges, K.V., 2000. Tectonics of the Himalaya and southern Tibet from two perspectives. Geol. Soc. Am. Bull. 112, 324–350.
Hodges, K.V., Walker, J.D., 1992. Extension in the Cretaceous Sevier orogen, North American Cordillera. Geol. Soc. Am. Bull. 104, 560–569.

Hodges, K.V., Parrish, R.R., Housh, T.B., Lux, D.R., Burchfiel, B.C., Royden, L.H., Chen, Z., 1992. Simultaneous Miocene extension and shortening in the Himalayan orogen. Science 258, 1466–1469.

Hodges, K.V., Parrish, R.R., Searle, M.P., 1996. Tectonic evolution of the central Annapurna Range, Nepalese Himalayas. Tectonics 15, 1264–1291.

Hodges, K.V., Hurtado, J.M., Whipple, K.X., 2001. Southward extrusion of Tibetan crust and its effect on Himalayan tectonics. Tectonics 20, 799–809.

Hoskin, P.W.O., Black, L.P., 2000. Metamorphic zircon formation by solid-state recrystallization of protolith igneous zircon. J. Metamorph. Geol. 18, 423–439.

Hubbard, M.S., 1989. Thermobarometric constraints on the thermal history of the Main Central thrust zone and Tibetan slab, eastern Himalaya. J. Metamorph. Geol. 7, 19–30.

Hubbard, M.S., Harrison, T.M., 1989. $^{40}Ar/^{39}Ar$ age constraints on deformation and metamorphism in the MCT Zone and Tibetan Slab, eastern Nepal Himalaya. Tectonics 8, 865–880.

Hurtado, J.M., Hodges, K.V., Whipple, K.X., 2001. Neotectonics of the Thakkhola graben and implications for recent activity on the South Tibetan Fault System in the central Nepal Himalaya. Geol. Soc. Am. Bull. 113, 222–240.

Jamieson, R.A., Beaumont, C., Medvedev, S., Nguyen, M.H., 2004. Crustal channel flows: 2. Numerical models with implications for metamorphism in the Himalayan–Tibetan orogen. J. Geophys. Res. 109, B06407. http://dx.doi.org/10.1029/2003JB002811.

Jamieson, R.A., Beaumont, C., Nguyen, M.H., Culshaw, N.G., 2007. Synconvergent ductile flow in variable-strength continental crust: numerical models with application to the western Grenville orogen. Tectonics 26, TC5005. http://dx.doi.org/10.1029/2006TC002036.

Jamison, W.R., 1996. Mechanical models of triangle zones. Bull. Can. Petrol. Geol. 44, 180–194.

Jessell, M.W., 1987. Grain-boundary migration microstructures in a naturally deformed quartzite. J. Struct. Geol. 9, 1007–1014.

Jessup, M.J., Cottle, J.M., Searle, M.P., Law, R.D., Newell, D.L., Tracy, R.J., Waters, D.J., 2008. P–T–t–D paths of Everest Series schist, Nepal. J. Metamorph. Geol. 26, 717–739.

Johnson, M.R.W., Oliver, G.J.H., Parrish, R.R., Johnson, S.P., 2001. Synthrusting metamorphism, cooling, and erosion of the Himalayan Kathmandu complex, Nepal. Tectonics 20, 394–415.

Jones, P.B., 1982. Oil and gas beneath east-dipping underthrust faults in the Alberta foothills. In: Powers, R.B. (Ed.), Geologic Studies of the Cordilleran Thrust Belt. Rocky Mountain Association of Geologists Bulletin 1, pp. 61–74.

Kali, E., Leloup, P.H., Arnaud, N., Mahéo, G., Liu, D., Boutonnet, E., Van der Woerd, J., Liu, X., Liu-Zeng, J., Li, H., 2010. Exhumation history of the deepest central Himalayan rocks, Ama Drime range: key pressure–temperature–deformation–time constraints on orogenic models. Tectonics 29, TC2014. http://dx.doi.org/10.1029/2009TC002551.

Kellett, D.A., Godin, L., 2009. Pre-Miocene deformation of the Himalayan superstructure, Hidden valley, central Nepal. J. Geol. Soc. Lond. 166, 261–275.

Kellett, D.A., Grujic, D., 2012. New insight into the South Tibetan detachment system: not a single progressive deformation. Tectonics 31, TC2007. http://dx.doi.org/10.1029/2011TC002957.

Kellett, D.A., Grujic, D., Erdman, S., 2009. Miocene structural reorganization of the South Tibetan detachment, eastern Himalaya: implications for continental collision. Lithosphere 1, 259–281.

Kellett, D.A., Grujic, D., Warren, C., Cottle, J., Jamieson, R., Tenzin, T., 2010. Metamorphic history of a syn-convergent orogen-parallel detachment: the South Tibetan detachment system, Bhutan Himalaya. J. Metamorph. Geol. 28, 785–808.

Khanal, S., Robinson, D.M., Kohn, M.J., Mandal, S., 2015. Evidence for a far-traveled thrust sheet in the Greater Himalayan thrust system, and an alternative model to building the Himalaya. Tectonics 34, 31–52.

King, J., Harris, N., Argles, T., Parrish, R., Zhang, H., 2011. Contribution of crustal anatexis to the tectonic evolution of Indian crust beneath southern Tibet. Geol. Soc. Am. Bull. 123, 218–239.

Kohn, M.J., 2008. PTt data from central Nepal support critical taper and repudiate large-scale channel flow of the Greater Himalayan Sequence. Geol. Soc. Am. Bull. 120, 259–273.

Kohn, M.J., Catlos, E.J., Ryerson, F.J., Harrison, T.M., 2001. Pressure–temperature–time path discontinuity in the Main Central thrust zone, central Nepal. Geology 29, 571–574.

Konstantinovskaia, E., Malavieille, J., 2005. Erosion and exhumation in accretionary orogens: experimental and geological approaches. Geochem. Geophys. Geosyst. 6, Q02006. http://dx.doi.org/10.1029/2004GC000794.

Kruhl, J.H., 1998. Reply: prism- and basal-plane parallel subgrain boundaries in quartz: a microstructural geothermobarometer. J. Metamorph. Geol. 16, 142–146.

Kruse, R., Stünitz, H., Kunze, K., 2001. Dynamic recrystallisation processes in plagioclase porphyroclasts. J. Struct. Geol. 23, 1781–1802.

Kuiper, Y.D., Williams, P.F., Kruse, S., 2006. Possibility of channel flow in the southern Canadian Cordillera: a new approach to explain existing data. In: Law, R., Searle, M.P., Godin, L. (Eds.), Channel Flow, Ductile Extrusion, and Exhumation in Continental Collision Zones. Geol. Soc. London Spec. Pub. 268, pp. 589–611.

Larson, K.P., Cottle, J.M., 2014. Midcrustal discontinuities and the assembly of the Himalayan midcrust. Tectonics 33, 718–740.

Larson, K.P., Godin, L., 2009. Kinematics of the Greater Himalayan Sequence, Dhaulagiri Himal: implications for the structural framework of central Nepal. J. Geol. Soc. Lond. 166, 25–43.

Larson, K.P., Godin, L., Davis, W.J., Davis, D.W., 2010a. Out-of-sequence deformation and expansion of the Himalayan orogenic wedge: insight from the Changgo culmination, south central Tibet. Tectonics 29, TC4013. http://dx.doi.org/10.1029/2008TC002393.

Larson, K.P., Godin, L., Price, R.A., 2010b. Relationship between displacement and distortion in orogens: linking the Himalayan foreland and hinterland in Central Nepal. Geol. Soc. Am. Bull. 122, 1116–1134.

Larson, K.P., Gervais, F., Kellett, D.A., 2013. A P–T–t–D discontinuity in east-central Nepal: implications for the evolution of the Himalayan mid-crust. Lithos 179, 275–292.

Law, R.D., 1990. Crystallographic fabrics: a selective review of their applications to research in structural geology. In: Knipe, R.J., Rutter, E.H. (Eds.), Deformation Mechanisms, Rheology and Tectonics. Geol. Soc. Spec. Pub. 54, pp. 335–352.

Law, R.D., 2014. Deformation thermometry based on quartz c-axis fabrics and recrystallization microstructures: a review. J. Struct. Geol. 66, 129–161.

Law, R.D., Searle, M.P., Simpson, R.L., 2004. Strain, deformation temperatures and vorticity of flow at the top of the Greater Himalayan Slab, Everest massif, Tibet. J. Geol. Soc. Lond. 161, 305–320.

Law, R.D., Jessup, M.J., Searle, M.P., Francsis, M.K., Waters, D.J., Cottle, J.M., 2011. Telescoping of isotherms beneath the South Tibetan Detachment System, Mount Everest Massif. J. Struct. Geol. 33, 1569–1594.

Law, R.D., Stahr, D.W., Francsis, M.K., Ashley, K.T., Grasemann, B., Ahmad, T., 2013. Deformation temperatures and flow vorticities near the base of the Greater Himalayan Series, Sutlej Valley and Shimla Klippe, NW India. J. Struct. Geol. 54, 21–53.

Lawton, D.C., Spratt, D.A., Hopkins, J.C., 1994. Tectonic wedging beneath the Rocky Mountain foreland basin, Alberta, Canada. Geology 22, 519–522.

Le Fort, P., 1975. Himalayas: the collided range. Present knowledge of the continental arc. Am. J. Sci. A275, 1–44.

Le Fort, P., 1996. Evolution of the Himalaya. In: Yin, A., Harrison, T.M. (Eds.), The Tectonics of Asia. Cambridge University Press, New York, pp. 95–106.

Lee, J., Hacker, B.R., Wang, Y., 2004. Evolution of North Himalaya gneiss domes: structural and metamorphic studies in Mabja Dome, southern Tibet. J. Struct. Geol. 26, 2297–2316.

Leger, R.M., Webb, A.A.G., Henry, D.J., Graig, J.A., Dubey, P., 2013. Metamorphic field gradients across the Himachal Himalaya, northwest India: implications for the emplacement of the Himalayan crystalline core. Tectonics 32, 540–557.

Leloup, P.H., Mahéo, G., Arnaud, N., Kali, E., Boutonnet, E., Liu, D., Xiaohan, L., Haibing, L., 2010. The South Tibet detachment shear zone in the Dinggye area. Time constraints on extrusion models of the Himalayas. Earth Planet. Sci. Lett. 292, 1–16.

Lister, G.S., 1977. Discussion: crossed-girdle c-axis fabrics in quartzites plastically deformed by plane strain and progressive simple shear. Tectonophysics 39, 51–54.

Lister, G.S., Dornsiepen, U.F., 1982. Fabric transitions in the Saxony granulite terrain. J. Struct. Geol. 4, 81–92.

Lister, G.S., Hobbs, B.E., 1980. The simulation of fabric development during plastic deformation and its application to quartzite: the influence of deformation history. J. Struct. Geol. 2, 355–371.

Lister, G.S., Price, G.P., 1978. Fabric development in a quartz–feldspar mylonite. Tectonophysics 49, 37–78.

Lombardo, B., Pertusati, P., Borghi, S., 1993. Geology and tectonomagmatic evolution of the eastern Himalaya along the Chomolungma–Makalu transect. In: Treloar, P.J., Searle, M.P. (Eds.), Himalayan Tectonics. Geol. Soc. London Spec. Pub. 74, pp. 341–355.

Long, S., McQuarrie, N., 2010. Placing limits on channel flow: insights from the Bhutan Himalaya. Earth Planet. Sci. Lett. 290, 375–390.

Long, S., McQuarrie, N., Tobgay, T., Hawthorne, J., 2011. Quantifying internal strain and deformation temperature in the eastern Himalaya, Bhutan: implications for the evolution of strain in thrust sheets. J. Struct. Geol. 33, 579–608.

Mainprice, D.H., Bouchez, J.-L., Blumenfeld, P., Tubia, J.M., 1986. Dominant c slip in naturally deformed quartz: implications for dramatic plastic softening at high temperature. Geology 14, 819–822.

Martin, A.J., DeCelles, P.G., Gehrels, G.E., Patchett, P.J., Isachsen, C., 2005. Isotopic and structural constraints on the location of the Main Central thrust in the Annapurna Range, central Nepal Himalaya. Geol. Soc. Am. Bull. 117, 926–944.

Martin, A.J., Copeland, P., Benowitz, J.A., 2014. Muscovite $^{40}Ar/^{39}Ar$ ages help reveal the Neogene tectonic evolution of the southern Annapurna Range, central Nepal. In: Mukherjee, S., Carosi, R., van der Beek, P.A., Mukherjee, B.K., Robinson, D.M. (Eds.), Tectonics of the Himalaya: Geological Society, London, Special Publication 412. http://dx.doi.org/10.1144/SP412.5.

McDermott, J.A., Whipple, K.X., Hodges, K.V., van Soest, M.C., 2013. Evidence for Plio-Pleistocene north–south extension at the southern margin of the Tibetan Plateau, Nyalam region. Tectonics 32, 317–333.

McKenzie, N.R., Hughes, N.C., Myrow, P.M., Xiao, S., Sharma, M., 2011. Correlation of Precambrian–Cambrian sedimentary successions across northern India and the utility of isotopic signatures of Himalayan lithotectonic zones. Earth Planet. Sci. Lett. 312, 471–483.

McQuarrie, N., Long, S.P., Tobgay, T., Nesbit, J.N., Gehrels, G., Ducea, M.N., 2013. Documenting basin scale, geometry and provenance through detrital geochemical data: lessons from the Neoproterozoic to Ordovician Lesser, Greater, and Tethyan Himalayan strata of Bhutan. Gondwana Res. 23, 1491–1510.

Miller, C., Thoni, M., Frank, W., Grasemann, B., Klotzli, U., Guntli, P., Draganits, E., 2001. The early Palaeozoic magmatic event in the Northwest Himalaya, India: source, tectonic setting and age of emplacement. Geol. Mag. 138, 237–251.

Morgan, S., Law, R.D., 2004. Unusual transition in quartzite dislocation creep regimes and crystal slip systems in the aureole of the Eureka Valley–Joshua Flat–Beer Creek pluton, California: a case for anhydrous conditions created by decarbonation reactions. Tectonophysics 384, 209–231.

Mukherjee, S., Koyi, H.A., 2010. Higher Himalayan Shear Zone, Sutlej section: structural geology and extrusion mechanism by various combinations of simple shear, pure shear and channel flow in shifting modes. Int. J. Earth Sci. 99, 1267–1303.

Murphy, M.A., Copeland, P., 2005. Transtensional deformation in the central Himalaya and its role in accommodating growth of the Himalayan orogen. Tectonics 24, TC4012. http://dx.doi.org/10.1029/2004TC001659.

Murphy, M.A., Yin, A., 2003. Structural evolution and sequence of thrusting in the Tethyan fold-thrust belt and Indus-Yalu suture zone, southwest Tibet. Geol. Soc. Am. Bull. 115, 21–34.

Murphy, M.A., Saylor, J.E., Ding, L., 2009. Late Miocene topographic inversion in southwest Tibet based on integrated paleoelevation reconstructions and structural history. Earth Planet. Sci. Lett. 282, 1–9.

Myrow, P.M., Hughes, N.C., Paulsen, T.S., Williams, I.S., Parcha, S.D., Thompson, K.R., Bowering, S.A., Peng, S.C., Ahluwalia, A.D., 2003. Integrated tectonostratigraphic analysis of the Himalaya and implications for its tectonic reconstruction. Earth Planet. Sci. Lett. 212, 433–443.

Myrow, P.M., Hughes, N.C., Searle, M.P., Fanning, C.M., Peng, S.C., Parcha, S.K., 2009. Stratigraphic correlation of Cambrian–Ordovician deposits along the Himalaya: implications for the age and nature of rocks in the Mount Everest region. Geol. Soc. Am. Bull. 121, 323–332.

Paces, J.B., Miller, J.D., 1993. Precise U–Pb age of the Duluth Complex and related mafic intrusions, northeastern Minnesota: geochronological insights in physical, petrogenetic, paleomagnetic, and tectonomagmatic processes associated with the 1.1 Ga midcontinent rift system. J. Geophys. Res. 98, 13997–14013.

Parrish, R.R., Hodges, K.V., 1996. Isotopic constraints on the age and provenance of the Lesser and Greater Himalayan Sequences, Nepalese Himalaya. Geol. Soc. Am. Bull. 108, 904–911.

Passchier, C.W., Trouw, R.A.J., 2005. Microtectonics. Springer, Berlin (366 pp.).

Pêcher, A., 1989. The metamorphism in the central Himalaya. J. Metamorph. Geol. 7, 31–41.

Peternell, M., Hasalová, P., Wilson, C.J.L., Piazolo, S., Schulmann, K., 2010. Evaluating quartz crystallographic preferred orientations and the role of deformation partitioning using EBSD and fabric analyser techniques. J. Struct. Geol. 32, 803–817.

Price, R.A., 1986. The southeastern Canadian Cordillera: thrust faulting, tectonic wedging, and delamination of the lithosphere. J. Struct. Geol. 15, 21–36.

Pryer, L.L., 1993. Microstructures in feldspars from a major crustal thrust zone: the Grenville Front, Ontario, Canada. J. Struct. Geol. 15, 21–36.

Quigley, M., Yu, L., Liu, X., Wilson, C.J.L., Sandiford, M., Phillips, D., 2006. ^{40}Ar/^{39}Ar thermochronology of the Kampa Dome, southern Tibet: implications for tectonic evolution of the North Himalayan gneiss domes. Tectonophysics 421, 269–297.

Rai, S.M., Guillot, S., Le Fort, P., Upreti, B.N., 1998. Pressure–temperature evolution in the Kathmandu and Gosainkund regions, Central Nepal. J. Asian Earth Sci. 16, 283–298.

Raimondo, T., Collins, A.S., Hand, M., Walker-Hallam, A., Smithies, R.H., Evins, P.M., Howard, H.M., 2009. Ediacaran intracontinental channel flow. Geology 37, 291–294.

Rana, N., Bhattacharya, F., Basavaiah, N., Pant, R.K., Juyal, N., 2013. Soft sediment deformation structures and their implications for Late Quaternary seismicity on the South Tibet Detachment System, Central Himalaya (Uttarakhand), India. Tectonophysics 592, 165–174.

Ratschbacher, L., Frisch, W., Liu, G., Chen, C., 1994. Distributed deformation in southern and western Tibet during and after the India–Asia collision. J. Geophys. Res. 99, 19817–19945.

Reddy, S.M., Searle, M.P., Massey, J.A., 1993. Structural evolution of the High Himalayan gneiss sequence, Langtang Valley, Nepal. In: Treloar, P.J., Searle, M.P. (Eds.), Himalayan Tectonics. Geol. Soc. London Spec. Pub. 74, pp. 375–389.

Rivers, T., 2008. Assembly and preservation of lower, mid, and upper orogenic crust in the Grenville Province — implications for the evolution of large hot long-duration orogens. Precambrian Res. 167, 237–259.

Robinson, D.M., DeCelles, P.G., Garzione, C.N., Pearson, O.N., Harrison, T.M., Catlos, E.J., 2003. Kinematic model for the Main Central Thrust in Nepal. Geology 31, 359–362.

Robinson, D.M., DeCelles, P.G., Copeland, P., 2006. Tectonic evolution of the Himalayan thrust belt in western Nepal: implications for channel flow models. Geol. Soc. Am. Bull. 118, 865–885.

Rubatto, D., 2002. Zircon trace element geochemistry: partitioning with garnet and the link between U–Pb ages and metamorphism. Chem. Geol. 184, 123–138.

Rubatto, D., Hermann, J., Buick, I.S., 2006. Temperature and bulk composition control on the growth of monazite and zircon during low-pressure anatexis (Mount Stafford, Central Australia). J. Petrol. 47, 1973–1996.

Rubatto, D., Chakraborty, S., Dasgupta, S., 2012. Timescales of crustal melting in the Higher Himalayan Crystallines (Sikkim, Eastern Himalaya) inferred from trace element-constrained monazite and zircon chronology. Contrib. Mineral. Petrol. http://dx.doi.org/10.1007/s00410-012-0812-y.

Sapkota, J., Sanislav, I.V., 2013. Preservation of deep Himalayan PT conditions that formed during multiple events in garnet cores: mylonitization produces erroneous results for rims. Tectonophysics 587, 89–106.

Schelling, D., Arita, K., 1991. Thrust tectonics, crustal shortening, and the structure of the far-eastern Nepal, Himalaya. Tectonics 10, 851–862.

Schmid, S.M., Casey, M., 1986. Complete fabric analysis of some commonly observed quartz *C*-axis patterns. Geophys. Monogr. 36, 263–286.

Schmitt, A.K., Grove, M., Harrison, T.M., Lovera, O.M., Hulen, J., Walters, M., 2003. The Geysers–Cobb Mountain Magma System, California (part 1): U–Pb zircon ages of volcanic rocks, conditions of zircon crystallization and magma residence times. Geochim. Cosmochim. Acta 67, 3423–3442.

Searle, M.P., 2010. Low-angle normal faults in the compressional Himalayan orogen; evidence from the Annapurna–Dhaulagiri Himalaya, Nepal. Geosphere 6, 296–315.

Searle, M., Godin, L., 2003. The South Tibetan detachment and the Manaslu leucogranite: a structural reinterpretation and restoration of the Annapurna–Manaslu Himalaya, Nepal. J. Geol. 111, 505–523.

Searle, M.P., Parrish, R.R., Hodges, K.V., Hurford, A., Ayers, M.W., Whitehouse, M.J., 1997. Shisha Pangma leucogranite, South Tibetan Himalaya: field relations, geochemistry, age, origin and emplacement. J. Geol. 105, 295–317.

Searle, M., Simpson, R.L., Law, R.D., Parrish, R.R., Waters, D.J., 2003. The structural geometry, metamorphic and magmatic evolution of the Everest massif, High Himalaya of Nepal–South Tibet. J. Geol. Soc. Lond. 160, 345–366.

Searle, M.P., Law, R., Godin, L., Larson, K.P., Streule, M.J., Cottle, J., Jessup, M., 2008. Defining the Himalayan Main Central thrust in Nepal. J. Geol. Soc. Lond. 165, 523–534.

Selleck, B.W., McLelland, J.M., Bickford, M.E., 2005. Granite emplacement during tectonic exhumation: the Adirondack example. Geology 33, 781–784.

Simpson, C., Wintsch, R.P., 1989. Evidence for deformation-induced K-feldspar replacement by myrmekite. J. Metamorph. Geol. 7, 261–275.

Smart, K.J., Krieg, R.D., Dunne, W.M., 1999. Deformation behavior during blind thrust translation as a function of fault strength. J. Struct. Geol. 21, 855–874.

Spencer, C.J., Harris, R.A., Dorais, M.J., 2012. The metamorphism and exhumation of the Himalayan metamorphic core, eastern Garhwal region, India. Tectonics 31, TC1007. http://dx.doi.org/10.1029/2010TC002853.

Srivastava, P., Mitra, G., 1994. Thrust geometries and deep structure of the outer and lesser Himalaya, Kumaon and Garhwal (India): implications for evolution of the Himalayan fold-and-thrust belt. Tectonics 13, 89–109.

Stacey, J.S., Kramers, J.D., 1975. Approximation of terrestrial lead isotope evolution by a two-stage model. Earth Planet. Sci. Lett. 26, 207–221.

Steck, A., Spring, L., Vannay, J.-C., Masson, H., Bucher, H., Stutz, E., Marchant, R., Tieche, J.-C., 1993. The tectonic evolution of the Northwestern Himalayan in eastern Ladakh and Lahul, India. In: Treloar, P.J., Searle, M.P. (Eds.), Himalayan Tectonics. Geol. Soc. London Spec. Pub. 74, pp. 265–276.

Steck, A., Epard, J.L., Robyr, M., 1999. The NE-directed Shikar Beh Nappe: a major structure of the Higher Himalaya. Eclogae Geol. Helv. 92, 239–250.

Stipp, M., Stunitz, H., Heilbronner, R., Schmid, S., 2002a. The eastern Tonale fault zone: a natural laboratory for crystal plastic deformation of quartz over a temperature range from 250 to 700 °C. J. Struct. Geol. 24, 1861–1884.

Stipp, M., Stunitz, H., Heilbronner, R., Schmid, S., 2002b. Dynamic recrystallization of quartz: correlation between natural and experimental conditions, deformation mechanisms, rheology and tectonics: current status and future perspectives. In: De Meer, S., Drury, M.R., De Bresser, J.H.P., Pennock, G.M. (Eds.), Geol. Soc. London Spec. Pub. 200, pp. 171–190

Stöcklin, J., 1980. Geology of Nepal and its regional frame. J. Geol. Soc. 137, 1–34.

Stöcklin, J., and K.D. Bhattarai (1982), Photogeological map of part of central Nepal: Kathmandu, Ministry of Industry and Commerce, Department of Mines and Geology, scale 1:100, 000.

Thakur, V.C., 1998. Structure of the Chamba nappe and position of the main central thrust in Kashmir Himalaya. J. Asian Earth Sci. 16, 269–282.

Thakur, V.C., and B.S. Rawat (1992), Geologic map of Western Himalaya: Dehra Dun, India, Wadia Institute of Himalayan Geology, scale 1:1,000,000.

Tullis, J.A., Christie, J.M., Griggs, D.T., 1973. Microstructures and preferred orientations of experimentally deformed quartzites. Geol. Soc. Am. Bull. 84, 297–314.

Upreti, B.N., 1999. An overview of the stratigraphy and tectonics of the Nepal Himalaya. J. Asian Earth Sci. 17, 577–606.

Upreti, B.N., Le Fort, P., 1999. Lesser Himalayan crystalline nappes of Nepal: problem of their origin. In: Macfarlane, A., Quade, J., Sorkhabi, R. (Eds.), Himalaya and Tibet: Mountain Roots to Mountain Tops. Geol. Soc. Am. Spec. Paper 328, pp. 225–238.

Valdiya, K.S., 1980. Geology of Kumaun Lesser Himalaya. Wadia Institute of Himalayan Geology, Dehra Dun, India (291 pp.).

Vannay, J.-C., Grasemann, B., 1998. Inverted metamorphism in the High Himalaya of Himachal Pradesh (NW India): phase equilibria versus thermobarometry. Schweiz. Mineral. Petrogr. Mitt. 78, 107–132.

Vannay, J.-C., Hodges, K.V., 1996. Tectonometamorphic evolution of the Himalayan metamorphic core between the Annapurna and Dhaulagiri, central Nepal. J. Metamorph. Geol. 14, 635–656.

Vannay, J.-C., Steck, A., 1995. Tectonic evolution of the High Himalaya in Upper Lahul (NW Himalaya, India). Tectonics 14, 253–263.

Vannay, J.-C., Sharp, Z.D., Grasemann, B., 1999. Himalayan inverted metamorphism constrained by oxygen isotope thermometry. Contrib. Mineral. Petrol. 137, 90–101.

Vannay, J.C., Grasemann, B., Rahn, M., Frank, W., Carter, A., Baudraz, V., Cosca, M., 2004. Miocene to Holocene exhumation of metamorphic crustal wedges in the NW Himalaya: evidence for tectonic extrusion coupled to fluvial erosion. Tectonics 23, TC1014. http://dx.doi.org/10.1029/2002TC001429.

Wagner, T., Lee, J., Hacker, B.R., Seward, G., 2010. Kinematics and vorticity in Kangmar Dome, southern Tibet: testing midcrustal channel flow models for the Himalaya. Tectonics 29, TC6011. http://dx.doi.org/10.1029/2010TC002746.

Webb, A.A.G., 2013. Preliminary balanced palinspastic reconstruction of Cenozoic deformation across the Himachal Himalaya (northwestern India). Geosphere 9, 572–587.

Webb, A.A.G., Yin, A., Harrison, T.M., Célérier, J., Burgess, W.P., 2007. The leading edge of the Greater Himalayan Crystallines revealed in the NW Indian Himalaya: implications for the evolution of the Himalayan Orogen. Geology 35, 955–958.

Webb, A.A.G., Yin, A., Harrison, T.M., Célérier, J., Gehrels, G.E., Manning, C.E., Grove, M., 2011a. Cenozoic tectonic history of the Himachal Himalaya (northwestern India) and its constraints on the formation mechanism of the Himalayan orogen. Geosphere 7, 1013–1061.

Webb, A.A.G., Schmitt, A.K., He, D., Weigand, E.L., 2011b. Structural and geochronological evidence for the leading edge of the Greater Himalayan Crystalline complex in the central Nepal Himalaya. Earth Planet. Sci. Lett. 304, 483–495.

Webb, A.A.G., Yin, A., Dubey, C.S., 2013. U–Pb zircon geochronology of major lithologic units in the eastern Himalaya: implications for the origin and assembly of Himalayan rocks. Geol. Soc. Am. Bull. 125, 499–522.

Wells, M.L., 1997. Alternating contraction and extension in the hinterlands of orogenic belts: an example from the Raft River Mountains, Utah. Geol. Soc. Am. Bull. 109, 107–126.

White, L.T., Ireland, T.R., 2012. High-uranium matrix effect in zircon and its implications for SHRIMP U–Pb age determinations. Chem. Geol. 306, 78–91.

White, L.T., Ahmad, T., Ireland, T.R., Lister, G.S., Forster, M.A., 2011. Deconvolving episodic age spectra from zircons of the Ladakh Batholith, northwest Indian Himalaya. Chem. Geol. 289, 179–196.

Whitmeyer, S.J., Simpson, C., 2003. High strain-rate deformation fabrics characterize a kilometers-thick Paleozoic fault zone in the Eastern Sierras Pampeanas, central Argentina. J. Struct. Geol. 25, 909–922.

Wiedenbeck, M., et al., 2004. Further characterisation of the 91500 zircon crystal. Geostand. Geoanal. Res. 28, 9–39.

Wiesmayr, G., Grasemann, B., 2002. Eohimalayan fold and thrust belt: implications for the geodynamic evolution of the NW Himalaya (India). Tectonics 21, 1058. http://dx.doi.org/10.1029/2002TC001363.

Wilson, C.J.L., Russell-Head, D.S., Kunze, K., Viola, G., 2007. The analysis of quartz *c*-axis fabrics using a modified optical microscope. J. Microsc. 227, 30–41.

Wyss, M., Hermann, J., Steck, A., 1999. Structural and metamorphic evolution of the northern Himachal Himalaya, NW India (Spiti–eastern Lahul–Parvati valley traverse). Eclogae Geol. Helv. 92, 3–44.

Yakymchuk, C., Godin, L., 2012. Coupled role of deformation and metamorphism in the construction of inverted metamorphic sequences: an example from far-northwest Nepal. J. Metamorph. Geol. 30, 513–535.

Yin, A., 2006. Cenozoic tectonic evolution of the Himalayan orogen as constrained by along-strike variation of structural geometry, exhumation history, and foreland sedimentation. Earth Sci. Rev. 76, 1–131.

Yin, A., Taylor, M.H., 2011. Mechanics of V-shaped conjugate strike-slip faults and the corresponding continuum mode of continental deformation. Geol. Soc. Am. Bull. 123, 1798–1821.

Yin, A., Harrison, T.M., Murphy, M.A., Grove, M., Nie, S., Ryerson, F.J., Feng, W.X., Le, C.Z., 1999. Tertiary deformation history of southeastern and southwestern Tibet during the Indo-Asian collision. Geol. Soc. Am. Bull. 111, 1644–1664.

Yin, A., Dubey, C.S., Kelty, T.K., Webb, A.A.G., Harrison, T.M., Chou, C.Y., Célérier, J., 2010. Geologic correlation of the Himalayan orogen and Indian craton: part 2. Structural geology, geochronology, and tectonic evolution of the Eastern Himalaya. Geol. Soc. Am. Bull. 122, 360–395.

Yu, H., Webb, A.A.G., He, D., 2015. Extrusion vs. duplexing models of Himalayan mountain building 1: discovery of the Pabbar thrust confirms duplex-dominated growth of the northwestern Indian Himalaya since Mid-Miocene. Tectonics 34, 313–333. http://dx.doi.org/10.1002/2014TC003589.

Zhang, J., Santosh, M., Wang, X., Guo, L., Yang, X., Zhang, B., 2012. Tectonic of the northern Himalaya since the India–Asia collision. Gondwana Res. 21, 939–960.